Defect Creation in InGaAs/GaAs Multiple Quantum Wells:

Correlation of Crystalline and Optical Properties with Epitaxial Growth Conditions

by

Matthias Karow

A Thesis Presented in Partial Fulfillment
of the Requirements for the Degree
Master of Science

Approved July 2014 by the
Graduate Supervisory Committee:

Christiana Honsberg, Chair
Nikolai Faleev
Cun-Zheng Ning

ARIZONA STATE UNIVERSITY

August 2014

ABSTRACT

Multiple quantum well (MQW) structures have been employed in a variety of solid state devices. The InGaAs/GaAs material system is of special interest for many optoelectronic applications. This study examines epitaxial growth and defect creation in InGaAs/GaAs MQWs at its initial stage. Correlations between physical properties, crystal perfection of epitaxial structures, and growth conditions under which desired properties are achieved appear as highly important for the realization and final performance of semiconductor based devices.

Molecular beam epitaxy was utilized to grow InGaAs/GaAs MQW structures with a variation in deposition temperature T_{dep} among the samples to change crystalline and physical properties. High resolution x-ray diffraction and transmission electron microscopy were utilized to probe crystal properties, whereas photoluminescence spectroscopy evaluated optical response. An optimal growth temperature T_{dep}=505°C was found for 20% In composition. The density of 60° primary and secondary dislocation loops increased continuously at lower growth temperatures and reduced crystal perfection, as evaluated by lateral and vertical coherence lengths and diffuse scattering in reciprocal space maps. Likewise, the strength of non-radiative Shockley-Read-Hall recombination increased as deposition temperature was reduced. Elevated deposition temperature led to InGaAs decay in the structures and manifested in different crystalline defects with a rather isotropic distribution and no lateral ordering. High available thermal energy increased atomic surface diffusivity and resulted in growth surface instability against perturbations, manifesting in lateral layer thickness undulations. Carriers in structures grown at elevated temperature experience localization in local energy minima.

InGaAs/GaAs MQW structures reveal correlation between their crystal quality and optical properties. It can be suggested that there is an optimal growth temperature range for each In composition with high crystal perfection and best physical response.

Es ist das Gefühl der Bewunderung, das uns gefangen nimmt, so oft wir erfahren, wie die Wirklichkeit einem logischen Gedankengebäude sich fügt. [1]

ACKNOWLEDGMENTS

Special thanks is given to my advisor Dr. Christiana Honsberg, who strongly supported me as Director of the QESST ERC throughout my affiliation with ASU in many ways. I also deeply appreciate to have built close mentoring relationships to Dr. Nikolai Faleev and Dr. Cun-Zheng Ning, who both continuously excited and encouraged me during my work process. Their patience in the discussion of encountered problems and experimental results influenced my work very positively. Further, I would like to say thanks to all QESST scholars and faculty for a great work atmosphere, which is characterized by an outstanding spirit and constructive cooperation. I will always be grateful to Rebecca Davis and Dr. Stephen Goodnick, who eased the transition to Arizona and have continuously supported me in all circumstances.

Please let me also thank the research group of Prof. Dr. Angela Rizzi, University of Göttingen, Germany and the OSRAM OS Company, Regensburg, Germany for pivotal technical support, as well as Dr. David Smith, Department of Physics, Arizona State University, for providing transmission electron micrographs along with their interpretation. Most valuably, I am very grateful for the sustaining and strong support from my family and friends, which has been crucial for all steps undertaken.

TABLE OF CONTENTS

Page

CHAPTER Page

LIST OF TABLES

Table Page

LIST OF FIGURES

Figure Page

Figure Page

Figure Page

Figure Page

Figure Page

Figure Page

LIST OF ACRONYMS

AES – Auger electron spectroscopy: Surface sensitive characterization technique for element determination

AVP – automated valve positioner: steers a needle valve to regulate the emitted flux from cracker cells as used for As in MBE setups

CF – confinement factor: ratio of modal gain to material gain in lasing structures

DL – dislocation loop: extended defect of both screw and edge type

FWHM – full width at half maximum: parameter expressing extent of peaked curves

HR-XRD – high resolution x-ray diffraction: non-destructive method for the analysis of crystalline structures, such as semiconductor crystals, based on interference of x-ray radiation, precise and highly sensitive setup allows to resolve fine structures (angles < 20 arc sec)

InGaAs – Indium-Gallium-Arsenide: Semiconducting ternary alloy of indium, gallium, and arsenic; a representative of element III-element V compound semiconductors

MBE – molecular beam epitaxy: ultra-high vacuum technique for growth of semiconductor crystals

MQW – multiple quantum well: the sequence of several SQWs

MSM – metal-semiconductor-metal: sandwich structure for metallic cavity nanolasers

ND – neutral density: refers to optical filters which exhibit constant attenuation over a wide range of wavelengths

OD – optical density: quantifies the degree of attenuation of optical filters in the reference wavelength range, optical power before P_{in} and after P_{out} passing a filter OD is related by $P_{out} = P_{in} \times 10^{-OD}$

PL – photoluminescence spectroscopy: optical technique in which light emitted from a sample upon photo excitation is collected and interpreted spectrally resolved

RC – rocking curve: x-ray diffraction scan in which detector position 2θ is kept constant and angle ω between source and sample is rocked around a diffraction value

RHEED – reflection high energy electron diffraction: a surface sensitive diffraction method commonly used for in-situ surface morphology monitoring during MBE growth

RSM – reciprocal space map: x-ray diffraction multi-scan with correlated variation of angles ω and 2θ, covering diffraction vectors of a specified area in reciprocal space

SPP – surface plasmon polariton: quasi-particle coupling photons confined to metal-dielectric interface with charge oscillations

SQW – single quantum well: a low band gap material layer embedded between comparatively higher band gap materials, acting as a confinement structure for carriers

SRH recombination – Shockley-Read-Hall recombination: non-radiative recombination type mediated by defect states with energies within the semiconductor band gap

TEM – transmission electron microscopy: microscopy technique with way increased resolution compared to conventional light microscope owing to the wave nature of electrons

UHV – ultra high vacuum: vacuum conditions with residual pressure on the order of 10^{-10} mbar

CHAPTER 1

INTRODUCTION

"It is impossible to imaging now modern solid-state physics without semiconductor heterostructures. Semiconductor heterostructures and, particularly, double heterostructures, including quantum wells, wires, and dots, are today the subject of research of two-thirds of the semiconductor physics community." [2]

This introduction to 2000 Nobel Laureate Zhores Alferov's Nobel lecture expresses the far reaching impact invention and experimental realization of semiconductor heterostructures have had on semiconductor science. This thesis is part of the strong research efforts on heterostructures as it is dedicated to the growth and characterization of periodic heterostructures composed of Indium-Gallium-Arsenide (InGaAs).

Early concepts of heterostructure devices used vertical changes in energy band gap to steer the charge carrier movement through quasi-electric fields [3] or to concentrate carriers in a particular volume of laser structures [4]. As soon as growth techniques became sophisticated enough to deposit layer thicknesses at which quantum-size effects appeared [5], the concept of heterostructuring enabled an unknown level of material and device design. It allowed to tailor fundamental semiconductor crystal properties, such as effective band gap energy, effective carrier masses, spatial carrier localization, and directional carrier mobility as needed for a proposed device. With this tool at hand, a plethora of heterostructure based devices has been developed, such as heterostructure light emitting diodes, high electron mobility transistors, quantum well lasers, and heterostructure solar cells resulting in omnipresent applications in modern communication, sensing, lighting, energy generation, and many more. [2, 6]

Despite the great success of heterostructure devices there are still wide research areas to be studied. The content of this thesis is such a one. Crystalline and physical properties of semiconductor materials can vary a lot depending on the epitaxial growth conditions used [7-10]. It is hence crucial for device design to consider correlations between physical properties, crystal perfection of epitaxial structures, and growth conditions under which desirable properties are achievable [11-14]. Suboptimal growth conditions may result in structural deteriorations, which in turn are able to degrade device operation [15-19]. This underlines the importance of the crystal structure as a determinant of device performance. This study aims to establish correlations between molecular beam epitaxy (MBE) growth conditions with crystalline and optical properties of InGaAs/GaAs multiple quantum well (MQW) structures.

The thesis is structured as follows. After an introduction to metallic cavity nanolasers as an application of InGaAs/GaAs MQW structures in Chapter 2, underlying concepts and theories for this work are presented in Chapter 3. The reader is familiarized with epitaxial growth by MBE and considerations on the creation of crystal defects. Two characterization techniques, high resolution x-ray diffraction and photoluminescence spectroscopy, are introduced and the examination of obtained data explained. A model relating light intensity collected in an excitation power dependent photoluminescence experiment with non-radiative trap state assisted recombination is proposed. Chapter 4 is dedicated to the experimental procedures and setups used, while Chapter 5 focusses on the experimental results obtained. Its outline resembles the interconnectedness of growth conditions, crystalline, and physical properties stressed in this work. Conclusions are eventually drawn in Chapter 6.

CHAPTER 2

APPLICATION OF INGAAS/GAAS MQWS

InGaAs/GaAs MQWs have a wide range of application, particularly in optoelectronic devices including photovoltaics and semiconductor lasers. Two frontiers in their individual research areas are MQW solar cells and nanolaser devices. The inclusion of MQWs into solar cells promises higher photo-conversion efficiency as compared to a p-n-junction cell. Enhanced optical absorption due to the two different bandgap energies involved increases the short-circuit current, while carrier confinement in the nanostructures increases the open-circuit voltage. [20-23]

In metallic cavity nanolasers, InGaAs/GaAs MQWs may serve as optically active region, providing superior material gain. Sufficient optical gain is a major concern in this type of lasing devices, as big losses due to adjacent metal layers must be compensated.

Nanolasers are coherent light sources with sizes comparable to or smaller than the wavelength emitted (volume $V < \lambda^3$). Wave guiding below the diffraction limit, however, cannot be realized with conventional laser cavity designs. Metallic cavities represent a promising approach to nanolasing devices. In such structures, the light field generated within a semiconducting gain medium is confined by surrounding metal layers, due to the strong interaction of photons with free electrons in the metal. The generation of such surface plasmon polaritons (SPPs) is particularly strong near a specific photon energy (SPP resonance), depending on the metal and geometry used. SPP coupling allows the effective photon wavelength within the gain medium to be reduced substantially from its vacuum value and hence enables optical confinement in small structures on the nanometer scale. The quasi-particle generation does, however, involve considerable optical losses,

particularly around the SPP resonance, which need to be compensated by sufficient material gain. In a trade-off approach, lasing modes need to be designed close to the resonance energy to achieve strong confinement, but also far enough to obtain losses which still can be overcome. It is beneficial that in metal-semiconductor-metal (MSM) waveguides, a particular design approach, the SPP generation and resultant optical confinement slows down the energy velocity of the light mode. This increases the gain per unit length experienced by an amplified mode and translates into superior modal gain, as compared to the usual situation of a plane wave in a uniform gain medium.[1] The large obtainable modal gain enables to overcome the optical losses.

MSM structures have the potential to reduce the size of semiconductor lasers below a few tens of nanometers by providing strong optical confinement, with a confinement factor CF > 1. Sufficient material gain in the semiconductor layers needs to overcome optical losses resultant from the SPP generation.

Nanolasers may be the key to integrated photonics in all-optical communication and data processing systems. Further, application in hybrid-integrated electronics to enable faster on-chip communication may become feasible due to a reduction in size mismatch between microelectronics and conventional optoelectronic devices. [24, 25]

First room temperature cw lasing under electrical injection has been demonstrated by *Ding et al.* [26] in a structure depicted in Fig. 1. The InGaAs gain medium is covered with silver to form the metallic cavity. The device ($V = 0.42\ \lambda^3$) has a threshold current of about 1000

[1] modal gain = material gain × confinement factor, SPP generation allows CF>1

μA and lases at 1554 nm (at 2040 μA) with a linewidth of 4 nm. Room temperature operation under electrical injection is of crucial importance for practical applications.

The incorporation of MQW structure in the gain medium may increase the material gain amplified by the SPP interaction and can potentially reduce threshold current and power consumption of nanolaser devices.

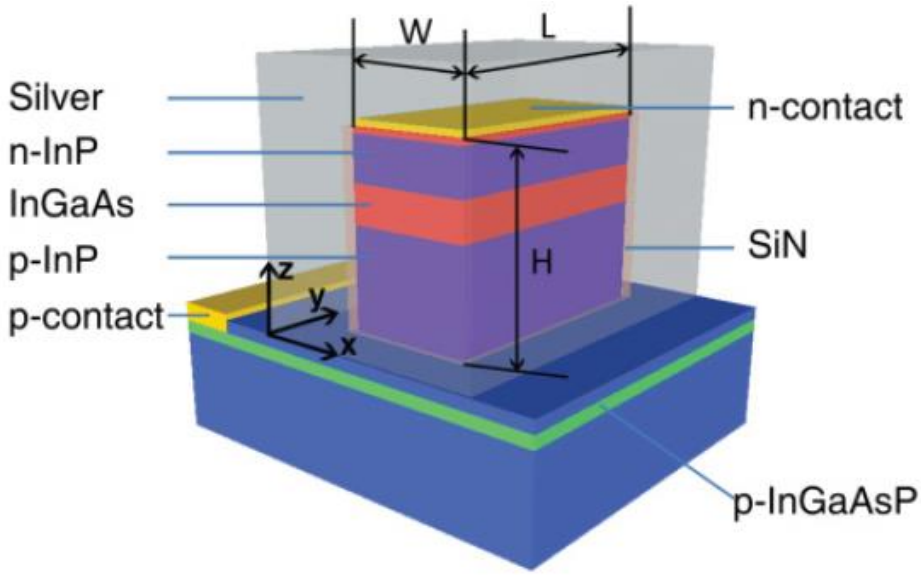

Fig. 1. Structure of a Metallic Cavity Nanolaser Capable of Room-Temperature CW Lasing under Electrical Injection. [26]

CHAPTER 3

BASIC PRINCIPLES

3.1. Epitaxial Growth by Molecular Beam Epitaxy

3.1.1 Method of MBE Growth

Molecular beam epitaxy (MBE) is an ultra-high vacuum (UHV) technique, which is used for the growth of monocrystalline semiconductor compounds. This growth technique excels in the purity of the obtained compound crystals and the sharpness of grown material interfaces. Both features are of special importance for the growth of device structures and for the analysis presented in this thesis. Impurities can readily act as undesired dopants or deep recombination levels and hence lead to unintended device performance, while sharp material interfaces can serve as charge carrier confinement regions, which are the heart of heterostructure devices. Abrupt material interfaces result from rather slow growth rates (typically 0.1 – 2.0 µm/hour) that allow to interrupt material supply with 2 - 3 monolayers precision and comparatively low growth temperatures leading to reduced interdiffusion at the interface. [27]

A typical MBE setup is sketched in Fig. 2, depicting the fundamental MBE components: UHV growth chamber, effusion cells with mechanical shutters, substrate holder, ion gauge, and cryopanels [28]. Elaborate vacuum equipment, such as turbomolecular pumps, cryopumps, and liquid nitrogen cooled cryopanels are required to maintain clean UHV conditions in the growth chamber. In effusion cells, mounted to the evacuated growth chamber, element-III source materials, such as Al, Ga, In are evaporated by a heat supply. Effusion orifices allow beams of atomic species to be directed onto a substrate on which the crystal growth is carried out. The effusion cell temperature is used to steer growth rates

and compound concentrations (relative arrival rates of molecular beams), as it strongly determines the emitted molecular fluxes. This is apparent from the solution of the applicable Clausius-Clapeyron equation (assume ideal Knudsen cell). The emitted atomic flux J_{MBE} is proportional to the vapor pressure p_{v} in the effusion cell

$$J_{\mathrm{MBE}} \propto \frac{p_{\mathrm{v}}}{\sqrt{T}} \propto \frac{1}{\sqrt{T}} \exp\left(-\frac{\Delta H_{\mathrm{vap}}}{RT}\right)$$

with the cell temperature T, the universal gas constant R, and the evaporation enthalpy ΔH_{vap} of the particular source material. This exponential behavior of J_{MBE} indeed represents a sensitive dependence on the cell temperature T [29]. Element-V materials, such as As or Sb are emitted from valved cracker cells, which provide small-molecular species, e.g. As_2 to the growth chamber. Their fluxes are varied by a needle valve at the crucible outlet. Mechanical shutters in front of each single effusion cell can interrupt beam fluxes within

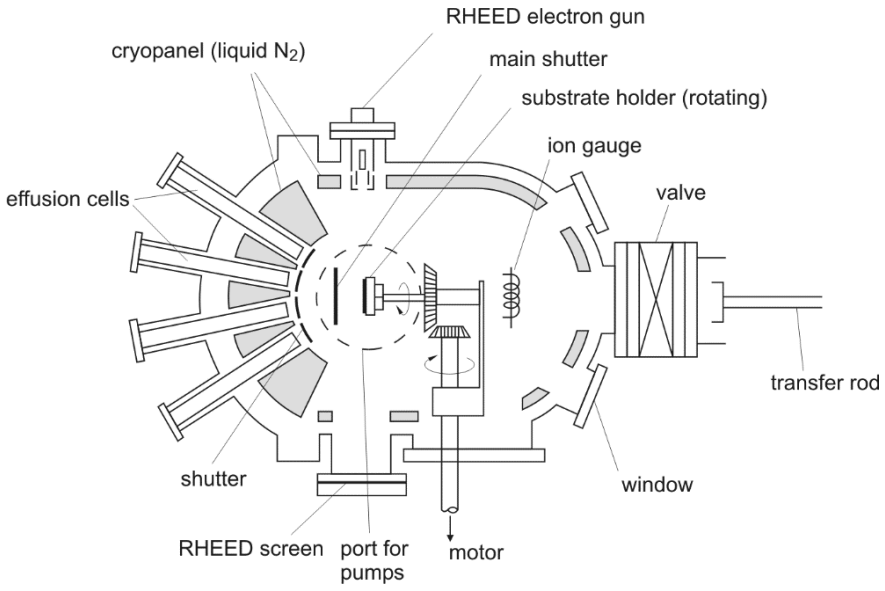

Fig. 2. Sketch of the Basic Constituents of a Typical MBE Setup. Not Shown Are Buffer and Intro Chamber Adjacent to the Growth Chamber, Which Serve as an Interlock System for the Insertion and Removal of Samples. [28]

fractions of a second and hence allow the growth of complex layer designs. For calibration purposes, the ion gauge (Beam Flux Monitor) can be exposed to the molecular beams in order to determine the beam equivalent pressure (BEP), a measure of the incident molecular flux, at various cell temperatures.

$$\ln(p_{\mathrm{BEP}}) = -\frac{\Delta H_{\mathrm{vap}}}{R} \cdot T^{-1} + C \ , \quad C \text{ a parameter}$$

Real MBE setups use Langmuir effusion cells, which operate at lower cell temperatures and feature bigger effusion holes, as compared to the ideal Knudsen cell for which the derivation is carried out. Slight deviations from the strict exponential dependence occur. In growth mode, the material beams are directed onto the substrate, a monocrystal with high crystalline quality, cut along a certain crystalline plane. Under favorable growth conditions the impinging atoms can migrate on and stick to the growth surface and finally crystallize, forming the desired crystal structure. The crystallization process sensitively depends on the individual atomic fluxes, their ratio, the substrate temperature (deposition temperature T_{dep}), atomic migration lengths, and the constitution of the substrate surface. These parameters are among the growth conditions that can be varied in MBE.

The MBE technique will be utilized in the frame of this thesis to grow III-As heterostructures with layer thicknesses as small as 8 nm.

3.1.2 Defect Creation in Epitaxial Growth

Epitaxial growth aims to transfer the crystal structure and a certain lattice orientation of a substrate onto a deposited film. In case of III-As materials the underlying lattice structure is of zincblende type, representative of the cubic crystal system.

The crystallization process of atoms and molecules impinging on the growth surface is crucially determined by the growth parameters introduced in the previous section, occurrence of defects at the growth surface, the chemical interaction between film and substrate, and the initial elastic stress in the epitaxial structure. [27] Initial elastic stress is thereby a result of lattice mismatch between substrate and epitaxial layer. Atoms and molecules incident onto the growth surface can either be reflected or adsorbed. Once attached, they might migrate on the surface, be incorporated into the existent lattice, or nucleate with other adatoms. Sufficient kinetic energy of the adsorbed species might also lead to desorption from the growth surface, Fig. 3.

This crystallization process, particularly when growing strained layers, is inherently coupled with the creation of lattice defects. Crystalline defects are not limited to point defects, such as vacancies, interstitials, and anti-site defects; line defects, such as dislocations (edge or screw type) and dislocation loops (both edge and screw type); planar defects, such as stacking faults; and finally volume defects, such as voids and cracks.

An empirical model describing the creation and structural transformation of crystalline defects in epitaxial growth was recently proposed [32-34]. A chain of four sequential stages

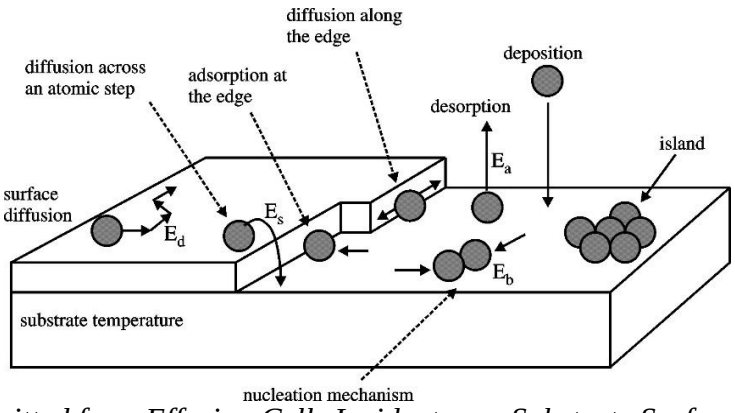

Fig. 3. Atoms Emitted from Effusion Cells Incident on a Substrate Surface Can Contribute to the Growth of a Film Via Several Mechanisms. [30]

was identified, which may be realized successively to accommodate elastic strain, aiming to stabilize the growth process. Each stage is characterized by specific preferred type of crystalline defects, their density and spatial distribution in the volume, and a certain extent of relaxation of initial elastic stress. The low deteriorate mode occurs in growth on high crystal quality epitaxial layers, such as single crystal substrates. It involves the creation of point defects, mixed type dislocation loops (60° dislocation loops in cubic structures), and partial relaxation of the initial elastic stress to the physical limit ~70%.

At the initial stage, point defects are created at the growth front, considerably enhanced under initial elastic stress. Inward diffusion of point defects into the epitaxial structures leads to accumulation in pre-dislocation clusters. Their induced local secondary stress finally triggers structural transformation of ripe clusters into primary dislocation loops

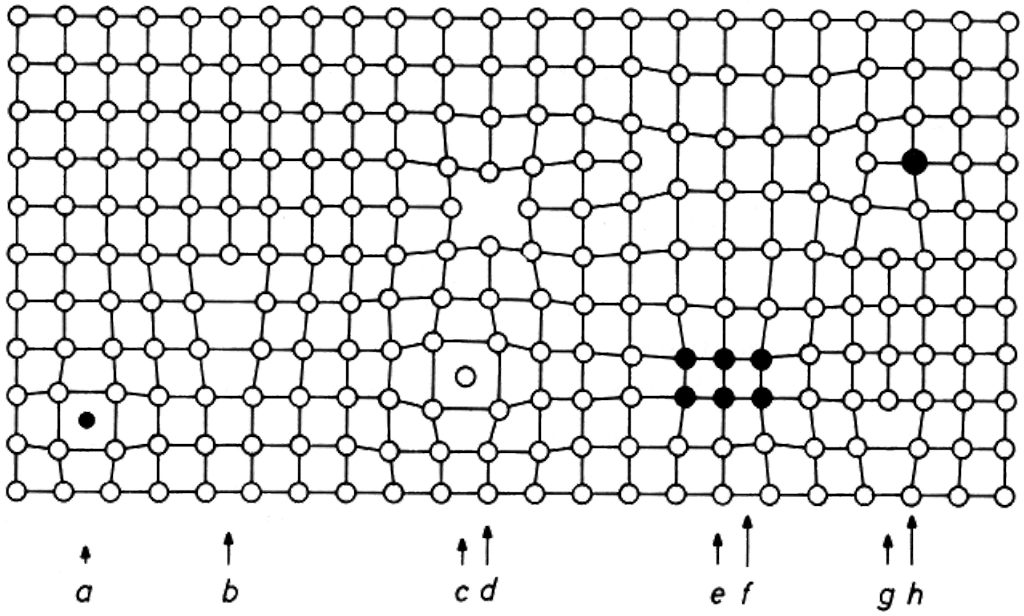

Fig. 4. Illustration of Particular Crystalline Defect Types A) Interstitial Impurity Atom, B) Edge Dislocation, C) Self Interstitial Atom, D) Vacancy, E) Precipitate of Impurity Atoms, F) Vacancy Type Dislocation Loop, G) Interstitial Type Dislocation Loop, H) Substitutional Impurity Atom [31]

(DLs). At this stage, such dislocation loops penetrate deeply into the substrate and form bottom closing edge segments there. Hence primary DLs do not contribute to relaxation of initial elastic stress (pseudomorphic growth). Most primary DLs will not have top edge segments, but follow the growth front and form wide trenches at the surface. Their dislocation extra planes enhance point defect inward diffusion. At this stage primary DLs (density 10^4 - $3 \cdot 10^6$ cm^{-2}) have reconstructed the growth front and rearranged spatial distribution of elastic stress.

Continued growth leads to further point defect inward diffusion and accumulation in clusters. A ripening process of pre-dislocation clusters results in the creation of 60° secondary DLs (density $10^7 - 7 \cdot 10^{10}$ cm^{-2}), which are smaller in spatial extent as compared to their primary counterparts. Initially these loops will exhibit a closing edge segment in the substrate and hence a significant fraction of secondary DLs does not contribute to relaxation of initial elastic stress either. Further point defect accumulations, however, will be concentrated around the epitaxial interface and lead to closing edge segment formation close to it. This marks the onset of stress relaxation by secondary DL edge segments. The extent of relaxation increases with the continued creation of edge segments close to the epitaxial interface, until the physical limit of ~70% for 60° dislocations is reached. Secondary dislocation loops are mainly realized as closed loops with top closing edge segments. Continued defect creation will shift the location of top edge segments away from the epitaxial interface into the epitaxial volume, which might be described as the formation of tertiary DLs. All three kinds of DLs may intersect in the volume at high DL densities resulting in the formation of Lomer dislocations.

Which stage might be finally realized does not only depend on growth parameters and elastic properties of the epitaxial films, but its sequential realization is also determined by the total thickness and multiplicity, in case of MQWs, of the epitaxial structure.

3.2. Assessing Crystalline Structure

It has been already pointed out that epitaxially grown semiconductor samples may exhibit slight deviations from an ideally perfect crystalline structure with unperturbed periodicity. Energy minimization and the thermodynamic trend of entropy maximization are accountable for this occurrence of sub-perfect atomic arrangement. In order to analyze structural properties on the scale of distances between crystal planes (GaAs: ~5.6 Å), the utilization of a probe with dimensions on the same order of magnitude is required. X-ray diffraction (XRD) (λ ~1.5 Å) has proven a reliable, non-destructive probe technique not only for the analysis of semiconductor crystals. In the following sections, the features found in XRD signals obtained from perfect crystals and specifically from semiconductor heterostructures will be introduced. Deviations from these optimal features will be related to extended defects created during epitaxial growth.

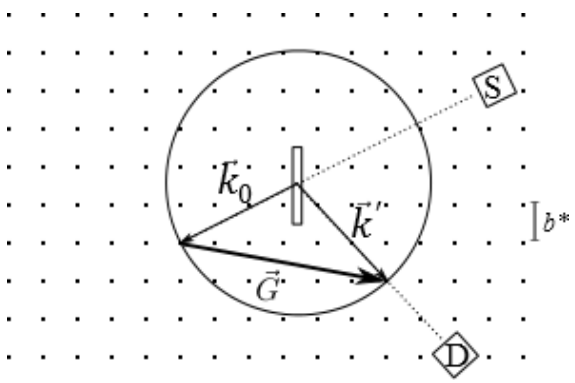

Fig. 5. The Ewald-Construction Provides a Pictorial Method to Meet the Coherent Diffraction Condition. S: X-Ray Source, D: Detector, Reciprocal Lattice Indicated.

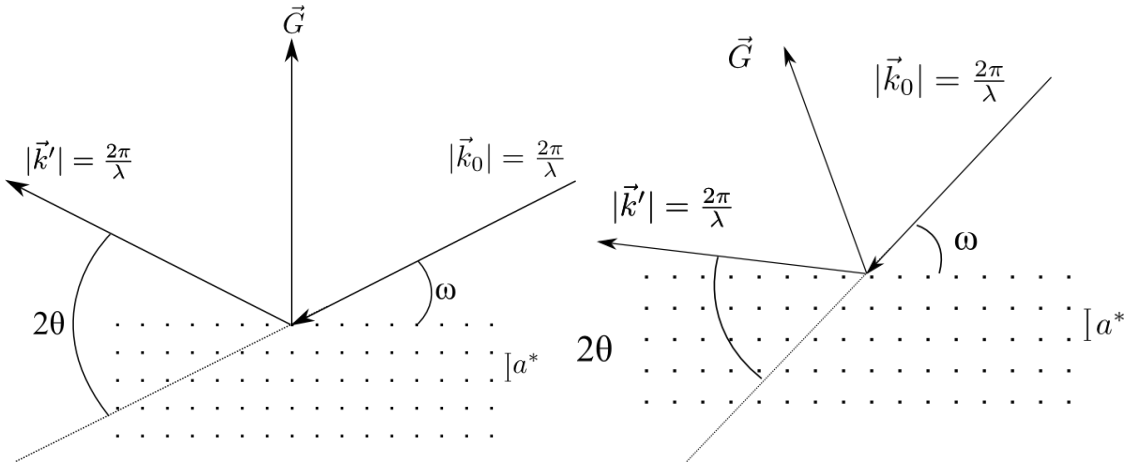

Fig. 6. Left: In a Specular ω-2θ Scan, the Diffraction Vector Is Perpendicular to the Epitaxial Crystal Plane and Thus to the Sample Surface (in This Work (001) Plane). For This Type of Scan Holds Δω/2Δθ=0.5 and ω=2θ/2. Information about Lattice Planes Parallel to the Sample Surface Can Be Obtained. Right: In a Generally Radial Scan, the Diffraction Vector Has a Non-Perpendicular Position. It Holds Δω/2Δθ=0.5 and in General ω≠2θ/2. The Diffraction Vector Can Be Decomposed into a Component with Information about Lattice Planes Parallel to the Sample Surface and Perpendicular to It.

3.2.1 High Resolution X-Ray Diffraction on Semiconductor Heterostructures

In an x-ray diffraction experiment, coherent x-ray waves are incident onto the sample under investigation. The angle of incidence can be varied continuously. The interaction of the x-ray waves with the periodic crystal structure in the sample gives rise to the emergence of x-ray radiation at several particular angles, depending on the specific type of crystal lattice. The Laue equations summarize the necessary angular conditions to be met for constructive interaction of x-rays with a crystalline structure. They can be expressed in the single term

$$\vec{k}_0 - \vec{k}' = \vec{G}$$

with the incident and emerging wave vector $\vec{k}_0$ and $\vec{k}'$, respectively, as well as a vector $\vec{G}$ of the reciprocal lattice. The reciprocal lattice can be understood as the Fourier transform

of the examined direct lattice. Hence every diffraction vector $\vec{G}$ can be obtained by a linear combination of the primitive reciprocal lattice vectors $\vec{b}_i$

$$\vec{G} = h\vec{b}_1 + k\vec{b}_2 + l\vec{b}_3$$

with the Miller indices *h k l*.

Along with the limitation for coherent scattering $|\vec{k}_0| = |\vec{k}'|$, a pictorial description of the diffraction condition can be given by the Ewald-construction, Fig. 5. The source S provides x-ray waves with the wave vector $\vec{k}_0$, pointing towards a point of the reciprocal lattice. A circle drawn around the starting point of $\vec{k}_0$ (sample position) indicates all possible final wave vectors satisfying the condition for coherent scattering. The reciprocal lattice vector $\vec{G}$ that starts at the tip of the incident wave vector and ends on the circle, defines a possible emerging wave vector $\vec{k}'$, satisfying the diffraction condition. [35]

Depending on the choice of diffraction vector $\vec{G}$ different structural features of the investigated sample can be extracted. The commonly used angles in diffraction experiments are shown in Fig. 6. In this viewgraph, the *ω-2θ* scan is introduced, from which the lattice plane spacing d_{hkl} perpendicular to the diffraction vector can be obtained.

$$d_{\mathrm{hkl}} = 2\pi/|\vec{G}_{\mathrm{hkl}}| \qquad (1)$$

This radial scan can be carried out with either the condition $\omega \neq 2\theta/2$ (asymmetric diffraction) or $\omega = 2\theta/2$ (symmetric diffraction).

For a comprehensive description the rocking ω scan will be introduced as well. It is commonly carried out after aligning onto a particular diffraction peak. While the detector position is kept fixed (*2θ*=const), ω is varied around its diffraction value. Measuring

contributions away from diffraction peaks in ω rocking curves gives insight into deteriorations in the sample. Details will be explained later in this section. [36]

Whereas the diffraction condition determines which angles between source, sample, and detector should result in constructive interference, it does not provide information about the strength of the signal. A more detailed description of the interaction between x-ray radiation and atoms in a crystal shows that the diffracted intensity is, among other influences, proportional to the square of the structure factor *F*

$$F = \sum_{\mathrm{j}} f_{\mathrm{j}}\, e^{2\pi i(hu_{\mathrm{j}}+kv_{\mathrm{j}}+lw_{\mathrm{j}})} \quad , \tag{2}$$

where the atomic factor f_{j} (Fourier transform of the electron distribution around an atom) for each atom sitting at the unit cell site $\vec{a}_{\mathrm{j}} = \begin{pmatrix} u_{\mathrm{j}} & v_{\mathrm{j}} & w_{\mathrm{j}} \end{pmatrix}$ was introduced. The underlying lattice structure of the material system of interest (InGaAs) is of zincblende type in this work. Calculating the strength of symmetric {001} diffractions by aid of Equation (2), one obtains a vanishing (001) signal, a weak (002) peak, and a strong (004) reflection. Hence, in a diffraction experiment the {001} plane spacing of an InGaAs compound is preferably obtained from the (004) reflex. [37]

Other features than the so far discussed Bragg peaks appear in *ω-2θ* scans obtained from heterostructures. Such structures contain several interfaces at which x-rays can be reflected forth and back. In perfect case, this requires the inclusion of multiple scattering events when calculating the diffraction pattern. The most accurate approach for high quality crystals is based on the *dynamical theory,* which aims to solve the wave equation in a periodic array of scattering centers. Analytical results from this theory are, however, limited to very particular cases. A trade-off between considering only single scattering

events as done in the previous paragraphs (*kinematical theory*) and the full description by the dynamical theory is given by the *semikinematical* approach. It can provide analytical expressions for *ω-2θ* scans measured on MQW structures. In the following a MQW structure, containing layer A and B grown pseudomorphically on material A is assumed. Each layer has the thickness t_A and t_B, respectively. The pattern of A on B is sequenced *N* times with the period $p = t_{A+} t_B$. Treating this structure in the semikinematical framework yields a diffraction intensity I_{MQW} stemming from the MQW structure

$$I_{\mathrm{MQW}} \propto \frac{(\Phi_{\mathrm{A}}\Phi_{\mathrm{B}})^N - 1}{\Phi_{\mathrm{A}}\Phi_{\mathrm{B}} - 1} \tag{3}$$

with the phase changes Φ_A and Φ_B upon crossing a single layer A or B, respectively. From this equation one can derive three prominent features:

1) The appearance of a zero order peak resultant from the MQW (0SL) at the angle

$$\omega_{0\mathrm{SL}} = \omega_{\mathrm{A}} - \frac{2\sin^2(\omega_{\mathrm{A}})}{\sin(2\omega_{\mathrm{A}})} \cdot \frac{t_{\mathrm{B}}}{t_{\mathrm{A}} + t_{\mathrm{B}}} \cdot \frac{a_{\perp,\mathrm{B}} - a_{\mathrm{A}}}{a_{\mathrm{A}}} \tag{4}$$

   with respect to the substrate Bragg peak at ω_A (see Equation (1)) and the vertical lattice constants a_i. Its position depends on the thickness of the individual layers, the vertical lattice constant, and thus on the compound composition.

   In fact, the 0SL peak appears at the angle where the Bragg peak of a single stressed layer with the average compound composition of the MQW would be found.

2) Additionally, satellite peaks with the angular distance $\Delta\omega_{SL}$ to the zero order can be found

$$\Delta\omega_{\mathrm{SL}} = m\frac{\sin(\omega_{\mathrm{A}})}{\sin(2\omega_{\mathrm{A}})} \cdot \frac{\lambda}{p} \quad , \quad m \in \mathbb{Z} \quad .$$

   The angular distance depends on the period *p* of the MQW structure.

Features 1) and 2) appear at the angles satisfying $(\Phi_A \Phi_B) = 1$ in Equation (3).

3) Further, faster oscillations arise from the $(\Phi_A \Phi_B)^N$ term. The distance of these interference fringes is given by

$$\Delta\omega_{\text{inter}} = \frac{\sin(\omega_A)}{\sin(2\omega_A)} \cdot \frac{\lambda}{Np}$$

and is hence dependent on the total MQW thickness *Np*. Between two neighboring satellite peaks, there will be *N-2* interference fringes. [36, 38]

From the position and spacing of the satellite peaks one can determine individual layer thicknesses and compound compositions. For the specific MQW design with *N=5* , $t_A = t_B$ =8 nm composed of $In_{0.2}Ga_{0.8}As$/GaAs grown pseudomorphically on a GaAs substrate and probed with λ=1.5406 Å (Cu-$K_{\alpha 1}$) one obtains:

$$\omega_{0SL} - \omega_{GaAs} = -0.52° = -31 \text{ arc min}$$

$$\Delta\omega_{SL} = 0.33° = 20 \text{ arc min}$$

$$\Delta\omega_{\text{inter}} = 0.066° = 3.9 \text{ arc min}$$

3 interference fringes between adjacent satellite peaks

Knowing these three angular distances one can identify individual layer thicknesses, material compositions, and the periodicity of the MQW structure.

3.2.2 Simulation of HR-XRD DC ω-2θ Scans

Grown samples may not exhibit perfect crystalline structure. Therefore, it would be helpful to calculate a theoretical ω-2θ scan as obtained from a perfect heterostructure that can then be compared to scans gathered from real samples. Although analytical expression cannot be obtained in the dynamical theory framework, numerical methods allow to use this more accurate approach. The commercial software package *X'Pert Epitaxy* (PANalytical) allows to enter structural parameters of a sample design and to then simulate the ω-2θ scan in dynamical framework [39]. Fig. 7 depicts the simulation of a symmetric ω-2θ scan around the GaAs (004) diffraction for the previously described structure. The previously explained

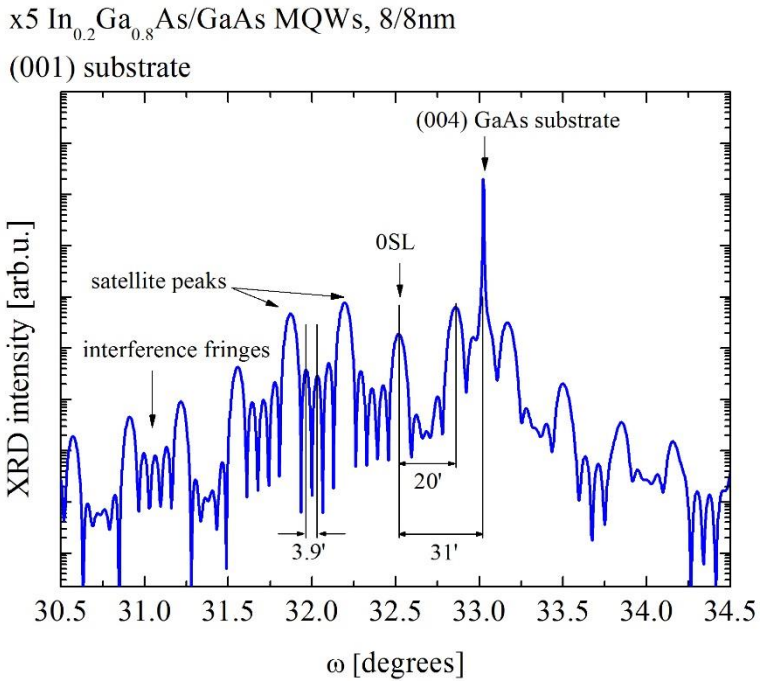

Fig. 7. Symmetric ω-2θ Scan Simulated for MQW Periodic Structure around the GaAs (004) Reflex. The MQW Structure Led to the Appearance of Both Satellite Peaks and Interference Fringes. Their Interspacing Is in Good Agreement with the Results Obtained from the Semikinematical Theory. (Units: 1' Stands for 1 Arc Min)

satellite peaks and interference fringes can be identified in the ω-2θ scan and their angular distance compared to the analytical results given in the last section.

On the other hand, layer thicknesses, periodicities, and concentrations of real structures can be obtained by reproducing their experimental HR-XRD curves.

3.2.3 Influence of Defects on HR-XRD Curves

Deviations from ω-2θ scans as simulated are mainly due to crystalline imperfections. The use of a sufficiently involved experimental setup, e.g. with respect to instrumental x-ray linewidth, is implied. Extended crystalline defects represent strong scattering centers at which the coherence of the scattered x-ray field may be destroyed. The resultant diffraction pattern will have contributions off the Bragg angles upon x-ray scattering at such imperfections. This leads to a broadening of diffraction peaks and to the appearance of diffuse scattering patterns. A loss in coherence diffuses interference fringes in ω-2θ scans resultant from a MQW structure, as these fine features critically depend on coherent interference throughout the entire structure and proper reflection at each interface.

Beside such qualitative comparisons, a quantitative evaluation can be done by calculating the vertical coherence length $L_{\text{vert.coh.}}$. In case of the vertical coherence of a MQW region, it is obtained from the linewidth Δω of a MQW peak in a symmetrical ω-2θ scan around the Bragg peak ω_B.

$$L_{\text{vert.coh.}} = \frac{0.9\lambda}{2\cos(\omega_B)} \cdot (\Delta\omega)^{-1} \approx \frac{8.263 \cdot 10^{-2}}{\Delta\omega/[\text{rad}]}\ \text{nm} \qquad (5)$$

The approximate expression holds for (004) diffraction. In case of zincblende structures, the vertical coherence is particularly diminished by closing edge segments in the volume

of an epitaxial structure, which can result from the intersection of two 60° dislocations. [32, 33]

Information about the density, type, and distribution of extended defects created in a sample can be gathered from ω-rocking curves (RC). A linewidth $\Delta\omega_{RC}$ of the coherent scattering peak obtained when rocking the angle ω can be interpreted as a density of dislocations N_{disl}. In case of 60° dislocation loops prominent in zincblende crystals an estimate is given by

$$N_{\mathrm{disl}} = \frac{\Delta\omega_{\mathrm{RC}}^2}{2\,\pi\,\ln(2) b^2} \tag{6}$$

where $\Delta\omega_{RC}$ is given in radians and b stands for the burgers vector [40]. The shape of the diffuse scattering pattern away from the coherent peak gives insight into the type and spatial lateral distribution of extended defects in the volume [41].

A combination of ω-2θ scans and ω RCs can be displayed in reciprocal space maps (RSM). Whereas a symmetrical ω-2θ scan is running along G_z in reciprocal space, ω-2θ/ω RSMs cover an area of scattering vectors with components G_z and G_x. They provide a pictorial representation of the entire diffuse scattering stemming from crystal deteriorations and thus can be utilized as a qualitative means to assess crystal quality. Whereas RSMs from perfect structures are composed of pointlike coherent scattering connected by a narrow surface truncation rod running along the G_z direction, crystal imperfections diminish pronunciation of this interconnection and contribute extended areas of diffuse scattering. Asymmetrical RSMs unveil the vertical and lateral lattice mismatch in heteroepitaxial structures. The lateral lattice mismatch reflects the degree of relaxation R of individual layers (Fig. 8), which can span the range from pseudomorphic (R=0) to almost entirely relaxed (R=1).

Layer relaxation is the result of dense dislocation creation. Referring to the model of the four stages of defect creation [32, 33] presented in section 3.1.2, relaxation involves the creation of dense and comparatively small secondary dislocation loops. They contribute a broad base of diffuse scattering around the coherent peak. Its full width at half maximum (FWHM) can serve as an estimate of their density via Equation (6).

This section introduced the high resolution x-ray technique as a means to study the crystalline properties of epitaxially grown semiconductor heterostructures. Several different experimental geometries, such as ω-2θ scans, ω rocking curves, and asymmetric reciprocal space maps, were presented and their individual importance for the examination of sample structure and crystalline properties highlighted. Besides qualitative comparisons

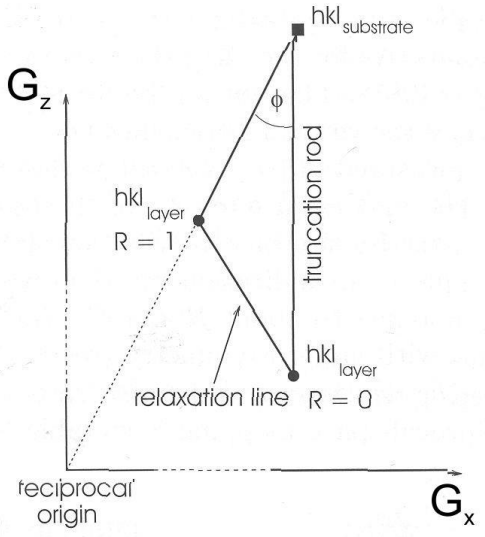

Fig. 8. From Asymmetrical Reciprocal Space Maps (RSM) the Degree of Lattice Relaxation of a Strained Film Can Be Revealed as a ΔG_x Shift. Same Scattering Vector G_x for Grown Film and Substrate Indicate Congruent In-Plane Lattice Constant and Thus a Lack of Relaxation (R=0). This Graph Shows a Compressively Strained Film. [36]

between a scattering response as expected from perfect structures and actually measured curves, quantitative conclusions can be drawn from the motivated equations.

3.3. Examination of Optical Properties

While the technique presented in the previous section is capable of analyzing density and distribution of extended defects created during epitaxial growth, it cannot definitely predict their impact on physical properties. In order to gain an understanding of how as grown structures might behave if applied in actual devices, the photoluminescence spectroscopy (PL) technique will be utilized. Spectra obtained by PL give insight into strength of optical loss paths, possible optical transitions, such as band edge emission or transitions between charge carrier confinement states, and their individual strength. These information, in turn, can be related to the structural features and specifically crystal deteriorations in the examined samples.

In a crystal lattice, the periodic arrangement of atoms leads to specific bands of energy states, which electrons can occupy. The band diagram, the one of GaAs is depicted in Fig. 9, exhibits energy ranges without electronic states and one particular gap is called the band gap E_g of the semiconductor. At vanishing temperature electrons fill up all states below this band gap (valence band) and all energy bands with higher energy are empty (conduction band).

In PL experiments, a monochromatic light source (laser or laser diode with a photon energy $\hbar\omega$ above expected transitions, such as $\hbar\omega > E_g$ band gap energy) excites electrons from the conduction into the valence band of a semiconductor crystal, by absorption of incident photons. Generated electron hole pairs can recombine via several different ways, roughly

categorized into radiative and non-radiative recombination, depending on if a photon is released or not. The emitted light is collected, spectrally resolved, and the obtained spectra analyzed with respect to position and intensity of identified peaks. More details on the used experimental setups will be presented in section 4.3.

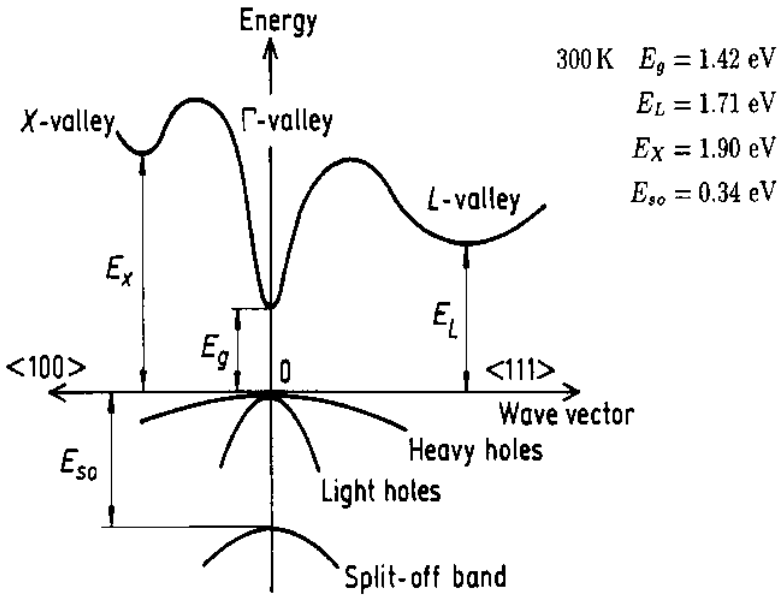

Fig. 9. Band Structure of the GaAs Crystal at Energies around the Band Gap at 300 K. Different States of Spin-Orbit Coupling Lift the Degeneracy of the Valence Band. At the Γ Point (Vanishing Wave Vector), However, Light Hole and Heavy Hole Bands Are Degenerate. [42]

3.3.1 Shockley-Read-Hall Recombination

One of the non-radiative types of electron hole pair recombination is mediated by energy states that lie within the band gap of a semiconductor crystal. Single carriers recombine with a trap site of a specific charge state. The released energy is transferred to multiple phonons generated. Strict lattice periodicity prohibits the existence of energy states in this energy range. Their appearance can be related to disruptions of a perfect lattice, e.g. by point defects, such as vacancies and interstitials, or dislocations. Any deviation from a

crystal periodicity has to lead to such energy states, as dictated by the underlying concept of quantum mechanically described electrons in perturbed periodic potentials. Another way to look at the formation of energy states within the band gap is the appearance of non-saturated (dangling) bonds at sites of crystalline defectiveness which can act as trap states. The carrier statistics of this recombination type, most commonly called Shockley-Read-Hall (SRH) recombination was derived by W. Shockley and W. Read [43] and experimentally studied by R. Hall [44]. Introducing the equilibrium densities n_0 and p_0 and carrier life times τ_n and τ_p for electrons and holes, respectively, as well as the carrier densities n_T and p_T at trap state energy, the net recombination rate per volume R_{SRH} is given by

$$R_{\mathrm{SRH}} = \frac{(n_0 + \Delta n)(p_0 + \Delta p) - n_T p_T}{\tau_p(n_0 + \Delta n + n_T) + \tau_n(p_0 + \Delta p + p_T)}.$$

The variables $\Delta n = \Delta p$ (electrons and holes are generated in pairs) describe excess carriers which may be generated by photo excitation in a photoluminescence experiment. This expression can be simplified by assuming undoped structures held at low temperature. As further $n_0 p_0 \propto \exp(-E_g/k_B T)$ and $n_T p_T \propto \exp(-E_g/k_B T)$ one can conclude for relevant E_g> 1.2 eV at 12 K that $n_0, p_0, n_T, p_T \ll \Delta n$. One thus obtains

$$R_{\mathrm{SRH}} = \frac{\Delta n}{\tau_n + \tau_p} =: A \cdot \Delta n$$

with the parameter A, classifying the strength of these transitions. The SRH recombination rate hence depends linearly on the excess carrier density, as it is in line with the nature of SRH recombination being a single particle process.

3.3.2 Radiative Recombination

Generated electron hole pairs can also recombine in a radiative band to band process. The thereby released energy ΔE is emitted as a photon at the wavelength $\lambda = {hc}/{\Delta E}$, (Planck constant h, speed of light c). There are two different kinds of radiative recombination, namely spontaneous and stimulated emission. Whereas spontaneous transitions involve only an excited electron hole pair, stimulated emission is induced by the interaction with an additional photon. The dominating process in a photoluminescence experiment is spontaneous emission, while stimulated emission is important in structures with carefully designed waveguides, such as laser diodes.

A detailed derivation of the spontaneous emission rate can be found in [45]. In the same limit of an undoped structure held at low temperature, as used before, the spontaneous recombination rate per volume R_{spo} can be determined as

$$R_{\mathrm{spo}} = B \cdot (\Delta n)^2 \ .$$

Hence, it turns out that the spontaneous recombination rate depends on the square of the excess carrier density. The parameter B, known as spontaneous emission coefficient is a measure of the strength of such transition and exhibits higher values in direct semiconductors, such as GaAs (Fig. 9) and InAs, as compared to indirect semiconductors, such as Si and Ge. By intuition, the square dependence reflects the nature of a two particle process. More details on the types of optical transitions available in semiconductor structures will be given in section 3.3.5.

3.3.3 Auger Recombination

The Auger-effect generally describes a non-radiative energy transfer between two electrons in an atomic shell. When an atom is excited, for instance by x-rays, lifting a shell electron, this electron can relax to its ground state and thereby transfer its energy to another shell-electron which thereupon leaves the atom as a so-called Auger-electron. This phenomenon was first observed and described by L. Meitner [46] and is nowadays applied as a spectroscopic technique (AES), which allows to determine chemical compositions of materials.

In semiconductor-respect the basic effect can be observed, too. The reading, however, deviates a little bit: Auger events involve nnp- (a hole and an electron recombine by transferring their energy to an additional electron) and npp-processes (excited hole) -transitions occur between bands. Further, the excited ("hot") carrier thermalizes by the emission of phonons.

This three particle process occurs at the rate

$$R_{\mathrm{Auger}} = C \cdot (\Delta n)^3$$

with the Auger coefficient *C* [45].

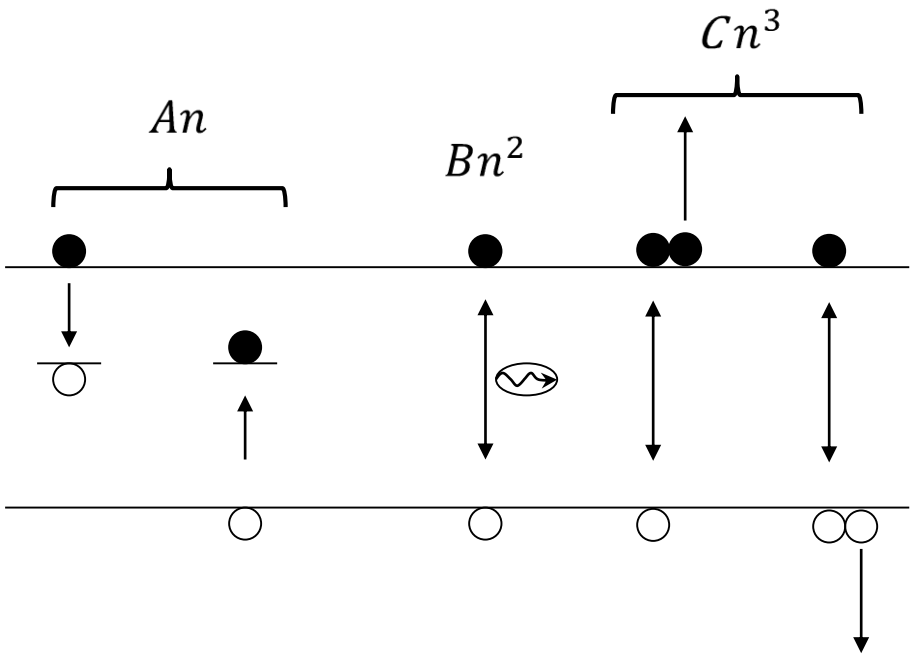

Fig. 10. Overview of Three Paths through Which Electron Hole Pairs Can Recombine.

3.3.4 Rate Equation for Excitation Power Dependent PL

In the previous sections, three different types of recombination mechanisms for electron hole pairs were introduced and their individual recombination rates (per volume) motivated. Now equations will be derived, which can describe the luminescent response emitted by semiconductor structures upon photo excitation. Incident laser light of wavelength λ and power *P* will lead to the generation rate *G* of electron hole pairs per sample volume *V*

$$G = \frac{\lambda P}{hcV}(1 - e^{-\alpha d}) \propto P$$

where the absorption coefficient α and the length of the absorption region *d* were introduced. As described before, these generated carriers can thereupon recombine via three different paths. This is expressed by the rate equation

$$\frac{\mathrm{d}n}{\mathrm{d}t} = G - An - Bn^2 - Cn^3 \ ,$$

in which n is used as excess carrier density ($n \approx \Delta n = \Delta p$) from now on.

The internal quantum efficiency IQE is introduced, in order to get a pictorial impression of the different regimes of recombination mechanisms. The definition counts radiative recombination events as beneficial processes, whereas both types of non-radiative recombination are non-beneficial.

$$\mathrm{IQE}: = \frac{Bn^2}{An + Bn^2 + Cn^3}$$

The general characteristic of the IQE as dependent on the pumping level is shown in Fig. 11. As this graph is intended to only reflect the overall shape of the IQE curve to be expected for an InGaAs sample, the following parameters were estimated, $\tau_{SRH}=A^{-1}$~10 ns (conservative estimate for 12 K), B~10^{-8} cm^3/s [47], and C~10^{-30} cm^6/s [48]. A steep

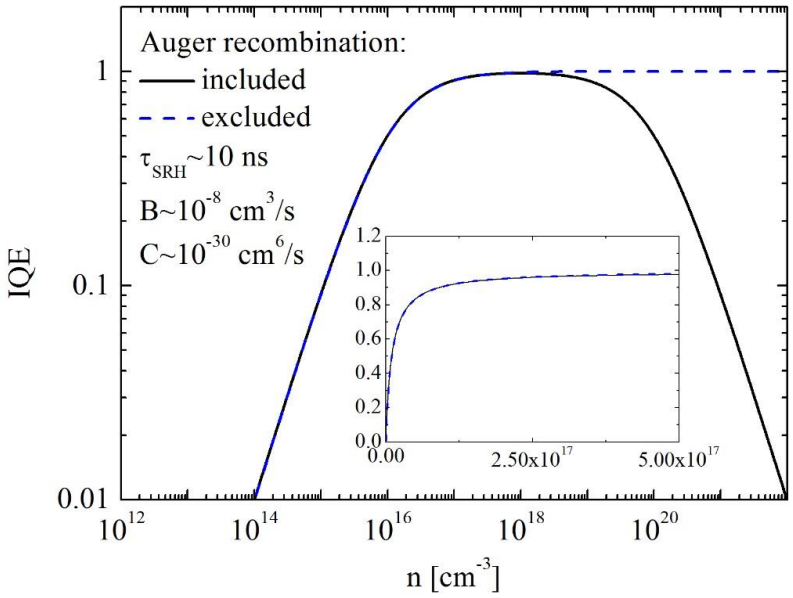

Fig. 11. Internal Quantum Efficiency IQE as Dependent on the Carrier Generation Rate G. The Inset Shows a Close Up onto the Low Excitation Range.

increase in IQE at low carrier densities *n* is followed by a plateau with maximal IQE. In this regime SRH-recombination becomes less and less important and the radiative recombination dominates finally. Further increase in excitation power leads to an IQE decrease, as the non-radiative Auger recombination type becomes stronger. The plot also contains the IQE curve for the case of vanishing Auger recombination, which coincides with the curve based on the full equation until the onset of the IQE decrease. It can be concluded that at low and intermediate generation rates *G*, one can enter a recombination regime, which can be described by SRH- and radiative recombination only. Making use of this limit of low excitation, the rate equation at steady state simplifies to

$$0 = n^2 + \frac{A}{B}n - \frac{G}{B} \ ,$$

which can be solved for the excess carrier density

$$n = -\frac{A}{2B} + \sqrt{\left(\frac{A}{2B}\right)^2 + \frac{G}{B}} \, .$$

Under these conditions the rate of photons $\dot{\varphi}$ emitted from a sample with the optical volume *V* is given by

$$\dot{\varphi}(G) = V\ B\ n^2 = VB\left[-\frac{A}{2B} + \sqrt{\left(\frac{A}{2B}\right)^2 + \frac{G}{B}}\right]^2 \qquad (7)$$

A sample plot of this equation in depicted in Fig. 12 (black, solid). The obtained curve may represent the light intensity emitted from a sample in an excitation power dependent PL experiment. Two different regimes can be identified, depending on the excitation power.

Regime (I): At low pumping level, only a small portion of the electron hole pairs recombines radiatively, but rather saturates trap states in the sample. The PL intensity

scales with the square of the excitation power. Equation (7) can be approximated in the limit $BG/A^2 \ll 1$ as

$$\dot{\varphi} = V\frac{B}{A^2}G^2 \propto G^2 \ .$$

Regime (II): At high enough excitation, trap states are mainly saturated and recombination occurs predominantly radiatively. The emitted PL intensity depends linearly on the excitation level. In this limit of $n \approx \sqrt{G/B}$, Equation (7) can be approximated as

$$\dot{\varphi} = VG \propto G$$

The transition between these two distinct regimes occurs continuously $\dot{\varphi} \propto G^k$, with a gradual decrease of the scaling parameter $k \in (1,2)$. A particular value of the power at which the transition occurs can be defined as the excitation level G_T at which the curves, approximated in the individual limits, intersect $VBG_\mathrm{T}^2/A^2 = VG_\mathrm{T}$. Since the generation rate at this point is given by

$$G_\mathrm{T} = \frac{A^2}{B} \propto A^2$$

the pumping level at which the transition from regime (I) to (II) occurs can be used as a measure of the magnitude of the *A* parameter and hence of the strength of trap states in the investigated sample.

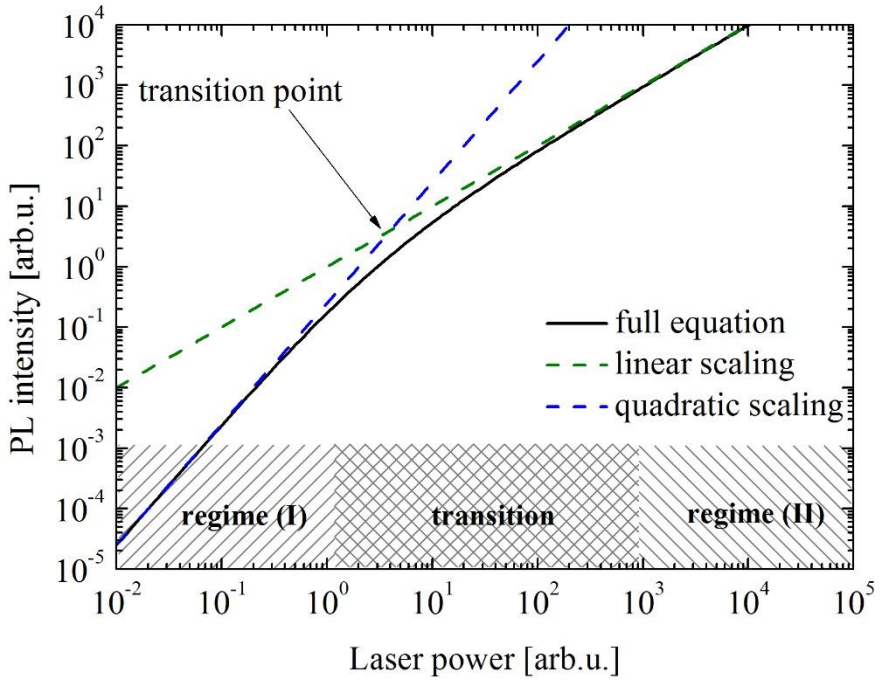

Fig. 12. Sample Curve of Emitted Spontaneous Radiation upon Varied Excitation Power. One Can Distinguish Two Different Regimes of Linear and Quadratic Scaling, Respectively.

In the previous four sections, the different recombination paths for excited electron hole pairs were introduced and specifically the dependence of their transition rate on the pumping level presented. Based on these dependencies, a model describing the light output in an excitation dependent PL experiment was created. Two major findings shall be summarized: (i) the PL intensity scales with the square of the excitation power at low pumping level and changes into a linear regime at higher laser power (ii) the stronger non-radiative SRH-recombination, the higher is the excitation power at which this transition occurs. This dependence shall assist to evaluate sample quality with respect to structural features affecting carrier dynamics.

3.3.5 Optical Transitions in Semiconductor Heterostructures

Optical recombination appears as a vertical transition in energy band diagrams (see Fig. 9). The reason being that the momentum of a photon (λ~1 µm → $p_{ph}=h/\lambda \sim 10^{-27}$ kg m/s) is vanishingly small as compared to the scale of carrier momenta in a crystal (GaAs: a~0.5 pm → at the edge of 1st Brillouin zone*:* $p_e=h/a \sim 10^{-22}$ kg m/s, five orders of magnitude larger than p_{ph}). This is why in good approximation the latter does not change in optical transitions. In order to get an understanding of the optical properties of semiconductor heterostructures, a brief review on electronic properties in such structures will be given.

Whereas the solution of the stationary Schrödinger equation for electrons in the lattice periodic potential of a crystal $\hat{T}\, V(\vec{r}) = V(\vec{r})$

$$\hat{H}\,\psi = \left(-\frac{\hbar^2}{2m_0}\underline{\Delta} + \hat{V}\right)\psi = E\psi \quad , \qquad \left[\hat{H},\hat{T}\right] = 0 \tag{8}$$

can be described as quasi-free Bloch electrons $\psi_{\vec{k}}(\vec{r}) = u_{\vec{k}}(\vec{r})e^{i\vec{k}\cdot\vec{r}}$ (lattice periodic Bloch function $\hat{T}\, u_{\vec{k}}(\vec{r}) = u_{\vec{k}}(\vec{r})$) , the inclusion of semiconductor hetero-interfaces represents a restriction in carrier movement along at least one spatial direction. This restriction has far-reaching implications for the optical properties and shall be motivated in the following.

The sequence of different semiconductor materials requires a specific band edge alignment across their interfaces since, in general, crystals with two different band gap energies E_g and electron affinities χ are brought together. In a rough picture, the alignment happens by (i) alignment of the Fermi-level across the interface and (ii) retention of the interface-inherent band edge offsets. As an example, Fig. 13 (left) shows the resultant band edge diagram for a GaAs/InGaAs/GaAs sequence, a single quantum well (SQW). As the thickness of the embedded layer is typically chosen on the nanometer scale, this structure

causes the confinement of carriers in this quantum well. As a consequence, electrons and holes can no more be considered quasi-free, but occupy states quantized (quantum number *n*) along the growth direction *z*. The resultant wave function contains a quasi-free component along the interface (wave vector $\vec{k}_{\perp}$) and an envelope function $\chi_{\mathrm{n}}(z)$ as a result of the confinement.

$$\psi_{\vec{k}}^{(n)}(\vec{r}) = u_{\vec{k}}(\vec{r}) e^{i\vec{k}_{\perp}\cdot\vec{r}}\, \chi_{\mathrm{n}}(z)$$

For low quantum numbers *n*, the envelope function $\chi_n(z)$ describes a standing wave within the well and has a decaying component in the barrier material. In case of multiple quantum wells (MQWs), the evanescent components of each well may interact with each other and form an overall envelope function with, again, quantized energy values. In Fig. 13 (right), the band edge diagram along growth direction is shown for a $\times$ 5-MQW structure with all layers 8 nm thick and a sequence of $In_{0.2}Ga_{0.8}As$/GaAs. Further, the ground state (*n=1*) for the conduction and the heavy- and light- hole valence band are included.

Considering the optical response of such structures, the confinement of carriers implies transitions to occur between these discrete quantum states. Although there is a continuum of energy states available with wave vectors perpendicular to the growth direction, the relaxation process to the band edge occurs on a faster time scale than the photon emission and hence these quantum state energies are crucial for optical spectra. As the strength $R_{\mathrm{i,f}}$ of an optical transition between two states ψ_{i} and ψ_{f} is determined by the magnitude of the matrix element of the perturbing light field Hamiltonian $\widehat{H}_{\mathrm{opt}}$, $R_{\mathrm{i,f}} \propto |\langle\psi_i|\widehat{H}_{\mathrm{opt}}|\psi_f\rangle|^2$ [49], one can deduce that such optical transitions are specifically strong in which the quantum number *n* does not change (Δn=0), e.g. between the individual confinement ground states.

The resultant photon energy is then given by $\hbar\omega = E_\mathrm{g} + E_\mathrm{e}^{(n=1)} + E_\mathrm{h}^{(n=1)}$, with the confinement ground states $E_\mathrm{i}^{(n=1)}, i \in \{\mathrm{e}, \mathrm{h}\}$ for electrons and holes, respectively. [50]

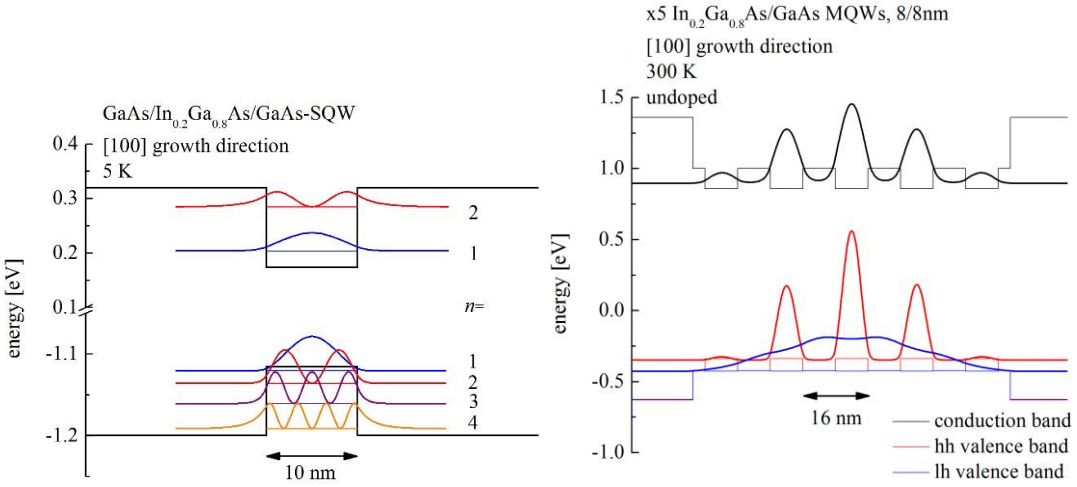

Fig. 13. Left: Embedding an InGaAs Layer Between Two GaAs Barriers Leads to a Band Edge Alignment That Represents a Quantum Well with Respect to the Potential Seen by Enclosed Carriers. Electrons and Holes in Such a Quantum Well Occupy Quantized (Quantum Number n) Energy Levels. (Conduction Band and Heavy Hole Valence Band Shown); Right: In a Sequence of Several QWs, the Carrier State Can Be Described by an Overall Envelope Function, Here Shown the Ground State n=1 for Conduction, Heavy Hole (HH) Valence, and Light Hole (LH) Valence Band. The Lifted Degeneracy of HH and LH Valence Band in the InGaAs Layers Is Due to Compressive Strain in Unrelaxed, Pseudomorphically Grown InGaAs on GaAs. [51]

DIGRESSION: Simulation of semiconductor heterostructures

After introducing the general notion of carrier confinement in semiconductor heterostructures and the basic equations dictating their electronic and optical properties, numerical methods which can determine band edges and envelope wave functions shall be presented briefly.

It is a hopeless endeavor to solve Equation (8) for all wave vectors $\vec{k}$ without any approximation. It is, however, feasible to get solutions with wave vectors around a particular point in reciprocal space, especially in optoelectronic context commonly chosen as the Γ point. Ground states for this particular value *k=0* can indeed be approximated numerically and small deviations from *k=0* are treated in the framework of perturbation theory with the perturbing Hamiltonian $\widehat{H}_{\mathrm{p}} = \frac{\hbar}{m_0}\vec{k}\cdot\hat{\vec{p}}$, where $\hat{\vec{p}}$ is the momentum operator. Details on numerical specifics can be found in [52].

Commercial software packages have been developed to solve for band edges, wave functions, confinement energies, and other properties in semiconductor structures, based on the introduced $\vec{k}\cdot\hat{\vec{p}}$- formalism. Among them, the nanodevice simulator *nextnano* [53] solves Poisson and Schrödinger equation in self-consistent manner. Whereas the Poisson equation describes the electric potential resulting from a particular charge distribution, the Schrödinger equation gets for the charge distribution in this very electric potential. This interconnectedness of both equations requires a self-consistent iteration scheme. Input parameters for *nextnano* include measures, compositions, and sequence of chosen materials, ambient temperature, the crystal plane of the underlying substrate, and applicable boundary conditions (here Neumann boundary conditions chosen for exclusion of transport phenomena beyond confinement region).

With this means at hand, the optical transition expected to be emitted from a perfect heterostructure in a PL experiment can be calculated. Both graphs in Fig. 13 were obtained with the *nextnano* nanodevice simulator.

CHAPTER 4

EXPERIMENTAL PROCEDURES

After reviewing theoretical aspects fundamental to this work, the utilized setups and experimental procedures will be introduced. So far it has been shown that HR-XRD and PL are suitable techniques to characterize crystalline and optical properties. This work aims to correlate them with chosen MBE growth conditions. MBE has been presented as a powerful technique for the growth of heterostructures with precise interfaces.

4.1. Molecular Beam Epitaxy

Epitaxial growth was carried out in the Solar Power Laboratory[2] with a VEECO GEN III MBE system. The growth chamber was equipped with a RHEED (reflection high energy electron diffraction) setup for in-situ monitoring of the surface morphology. Background pressure before growth was on the order of 10^{-9} torr. Undoped (001) GaAs wafers with an oxide capping were introduced to the growth chamber onto the substrate holder. Successive increase of sample holder temperature was monitored with RHEED and a pyrometer until deoxidation of the wafer occurred. Deoxidation is indicated by a change from a diffuse/spotty to a bright streaky RHEED pattern, as the surface morphology changes from an amorphous to a crystalline texture. The pyrometer was calibrated to the occurrence of deoxidation at T_{deox}=580°C. To complete the deoxidation process the sample was kept at 610°C for 15 min under As-overpressure. The entire growth process was carried out under As-rich conditions (As-cell cracker/bulk temperature was 960/405°C), so the growth rate

[2] Solar Power Laboratory, Arizona State University Research Park, 7700 S. River Parkway, Tempe, AZ 85284, USA

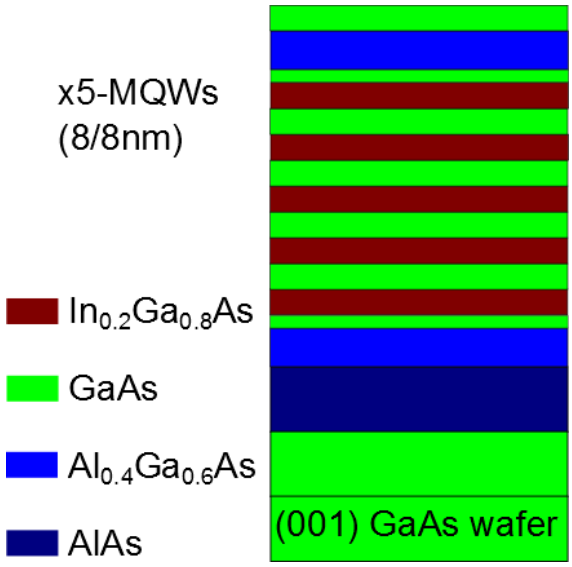

Fig. 14. Outline of the Grown Epitaxial Films, Not Drawn to Scale.

is determined by the incident element-III fluxes [27]. Further, the sample holder was kept rotating during the deposition process to ensure isotropic flux exposure. A 250 nm thick GaAs buffer layer was grown at T_{dep}=595°C at the growth rate R=1.63 Å/s (Ga-cell 1065/940°C)[3], in order to provide a smooth crystalline surface for the preceding epitaxial films, followed by a 100 nm thick AlAs layer. $Al_{0.4}Ga_{0.6}As$ (Al-cell 1106/1136°C, R=1.09 Å/s) cladding layers were grown 15 nm thick at the same deposition temperature T_{dep} surrounding an InGaAs/GaAs MQW structure. The latter was grown at reduced deposition temperature T_{dep}, see Table 1, under As supply BEP_{As}~$2 \cdot 10^{-6}$ torr (AVP=220). For this the GaAs (Ga-cell 1035/910°C) growth rate was kept at R=0.8 Å/s, while the InAs (In-cell 890/745°C) growth rate was intermittently kept at 0.2 Å/s during the InGaAs growth. Both, GaAs and InGaAs layers were grown 8 nm thick with a MQW periodicity of 5. After the

[3] Effusion cell temperatures given in the format (tip temperature/bottom temperature °C)

Table 1. Deposition Temperatures for the InGaAs/GaAs MQW Growth of Different Samples.

Sample ID	T_{dep} [°C]
G13-007	520
G13-009	490
G13-011	505
G13-013	475

growth, the sample cooled down under As exposure and was then removed from the growth chamber. The entire structure is depicted in Fig. 14. $In_{0.2}Ga_{0.8}As$ is lattice mismatched by 1.4% to GaAs.

4.2. High Resolution X-Ray Diffractometry

Crystalline properties were analyzed with a PANalytical X'Pert Pro Material and Research Diffractometer (Fig. 15) accessible through the LeRoy Eyring Center for Solid State Science[4]. It provides monochromatic Cu-$K_{\alpha 1}$ radiation (λ=1.5406 Å) of 19 arc sec divergence, which is formed by a ¼° divergence slit, a multi focusing mirror followed by

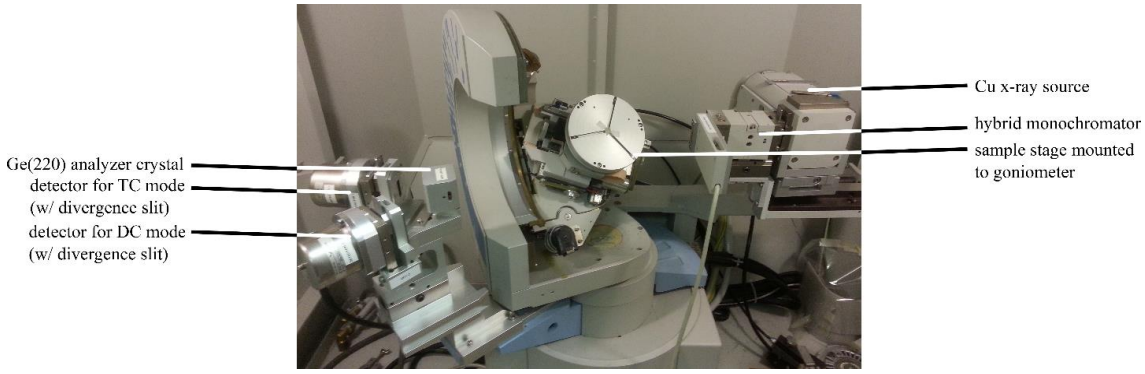

Fig. 15. PANalytical X'Pert Pro MR Diffractometer, Optical Scheme. LeRoy Eyring Center for Solid State Science.

[4] LE-CSSS, Arizona State University, 901 S. Palm Walk, Tempe, AZ 85287, USA

a four-bounce Ge(220) Hybrid monochromator. Double crystal ω-2θ scans were measured around the GaAs (004) reflection around ω=33.03° with a narrow ¼° receiving slit in front of the detector to diminish diffuse scattered background. For the acquisition of triple crystal ω-2θ scans and ω rocking curves (RC), a three bounce Ge(220) analyzer crystal was inserted between sample and detector (1° receiving slit) in order to spatially separate coherent and diffuse scattering. For ω RCs, the adequate ω and 2θ values of a certain reflex were taken from the previous ω-2θ scan. From there on the value ω was varied around the coherent scattering peak. Symmetric (004) and asymmetric (224) ω-2θ/ω reciprocal space maps were collected using the triple crystal diffraction geometry. Thereby the GaAs (224) reflection appears at ω=6.5°, 2θ=83.743°.

4.3. Photoluminescence Spectroscopy

4.3.1 Temperature Dependent PL

Temperature dependent photoluminescence spectroscopy was carried out in the laboratories of the research group "III-N based functional hetero- and nanostructures" led

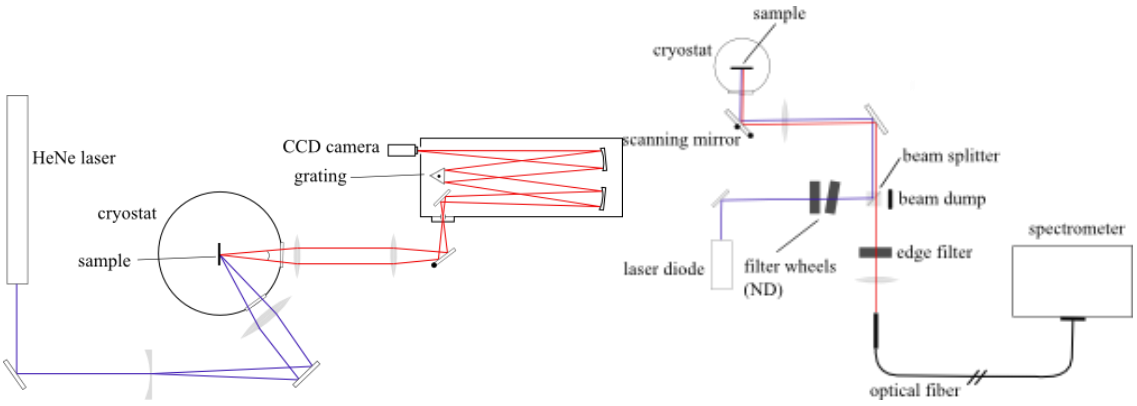

Fig. 16. Setups for Temperature Dependent (Left) and Excitation Power Dependent (Right) Photoluminescence Spectroscopy.

by Prof. Dr. Angela Rizzi[5], Göttingen University, Germany. The setup uses a 632.8 nm (1.96 eV) HeNe laser for photo excitation at 10 mW. The sample was mounted in a He flow cryostat (Oxford Instruments), evacuated by both a rough and a turbo molecular pump. Equipped with a sample heater, this control system allows the ambient temperature to be scanned between 5 and 300 K. The light emitted from the sample was dispersed in a grating spectrometer (Acton Research) and the signal collected with nitrogen cooled CCD camera (Princeton Instruments). Temperature increments of 25 K were perceived to sufficiently resolve the temperature behavior of the gathered PL signal.

4.3.2 Excitation Power Dependent PL

For excitation power dependent photoluminescence experiments, a setup of the Testing/Analytics Department of the OSRAM Opto Semiconductors[6] company was utilized. In this setup, the investigated samples were excited with a 376 nm (3.3 eV) laser diode (Toptica) at 70 mW maximal power. Since laser diodes emit a broad range of wavelengths apart from the actual laser line (spontaneous emission), a test spectrum was

Table 2. Optical Densities (OD) of the Used Neutral-Density Filters as Placed in the Two Filter Wheels.

position	**1**	**2**	**3**	**4**	**5**	**6**
filter wheel 1	0	1	2	-	-	-
filter wheel 2	0	0.3	0.5	0.6	0.9	1.3

[5] Prof. Dr. Angela Rizzi, Institut für Halbleiterphysik, Friedrich-Hund-Platz 1, 37077 Göttingen, Germany
[6] Dr. Roland Zeisel, Leibnizstraße 4, 93055 Regensburg, Germany

acquired with a bare sample holder to ensure that the obtained luminescence spectra contain only information about the measured sample (Fig. 17). Two independent filter wheels equipped with neutral density (ND) filters (Edmund Optics) allowed to vary the excitation density incident onto the sample by three orders of magnitude with increments of roughly optical density (OD) 0.3. Laser power before P_{in} and after P_{out} passing a single ND filter OD_1 is related by $P_{out} = P_{in} \times 10^{-OD_1}$. Table 2 lists the ODs as used in this experiment. The two filter wheels were tilted with respect to each other in order to minimize resonator effects, which otherwise result in excitation powers deviating from a linear superposition of the individual filters. The sample was kept at 12 K in a cryostat (Leybold Vakuum) cooled by a Gifford-McMahon chiller. Both rough and turbo molecular pumps evacuated

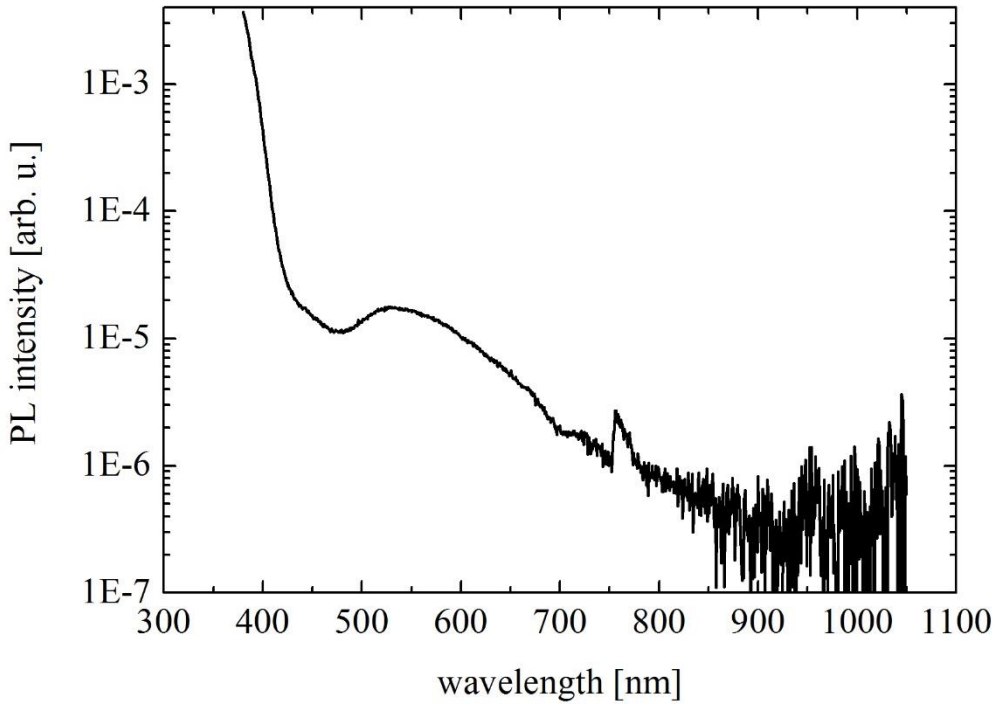

Fig. 17. Spectrum of Bare Sample Holder at Maximal Laser Diode Power. The Spectrum Contains a Broad Range of Spontaneous Radiation Emitted by the Laser Diode and a Second Order Diffraction Replica of the Laser Line at 750 nm (Cut by Edge Filter). Most Importantly, the Wavelength Range 850-1050 nm Exhibits a Signal below the Noise Level.

the cryostat. A grating spectrometer (Instrument Systems) separated different spectral contributions of the light emitted by the sample and projected it onto a CCD camera to record the obtained spectra. As the used type of spectrometer acquires data always for the entire detectable wavelength range, the intense laser peak was attenuated by a 376 nm edge filter (blocks light with wavelength < 376 nm) in order to prevent the CCD camera from being overexposed. [54]

CHAPTER 5

EXPERIMENTAL RESULTS

5.1. Analysis of Crystalline Properties

Crystalline properties of grown structures are deduced from high resolution x-ray experiments. Double crystal (DC) ω-2θ scans allow to determine layer thicknesses (vertical coherence length) and compound compositions, as pointed out in section 3.2.2. Experimental results collected around the (004) GaAs reflection are shown for all examined structures in Fig. 18. Aside from the intense (004) GaAs peak, the curves are dominated by SL peaks and fast interference fringes related to the total thickness of a MQW structure. Equal angular spacing between adjacent SL peaks for all samples results from a SL-period ~16 nm. The occurrence of three fast interference fringes between adjacent SL peaks reveals a ×5 multiplicity of the MQW structure. Their angular spacing corresponds

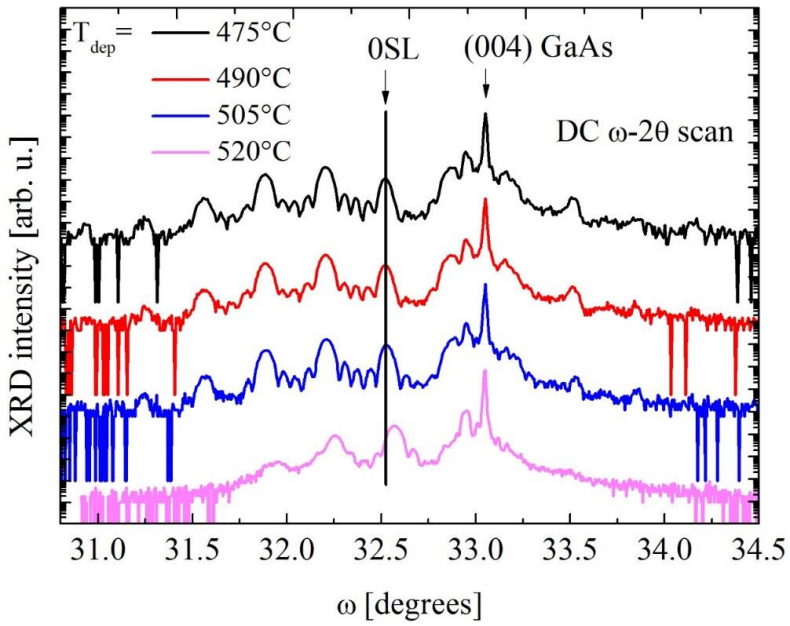

Fig. 18. DC ω-2θ Scans Collected in the Vicinity of the (004) GaAs Reflection for All Samples, 475°C ≤ T_{dep} ≤ 520°C.

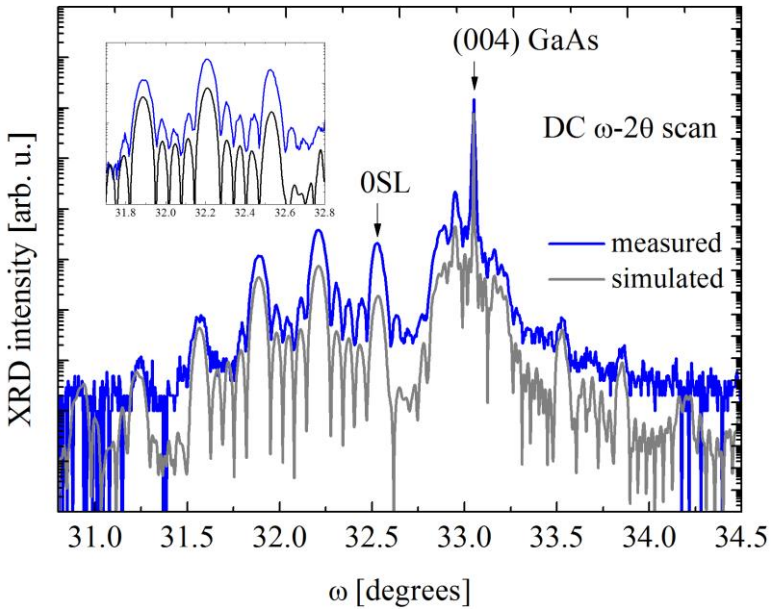

Fig. 19. DC ω-2θ Scan of the Structure Grown at T_{dep}=505°C along with a Simulation Used to Obtain Layer Thicknesses and Compound Compositions.

to a total MQW thickness ~80 nm. The 0SL peak, related to the mean SL composition, appears at the same angular position for all samples T_{dep}≤505°C corresponding to an In composition ~20% in the InGaAs layers. The shift of the 0SL peak to higher diffraction angles for T_{dep}=520°C is indicative for an In concentration ~18.5%. All experimental DC ω-2θ scans were simulated (see section 3.2.2) in order to determine correct In compositions and layer thicknesses, as exemplarily shown in Fig. 19. The parameters obtained from these simulations and quantitative results from examinations described later in this section are listed in Table 3. The accuracy of these simulation results was found to be ~0.2% for compositions and ~0.2 nm for layer thicknesses. With regard to crystal quality, the samples T_{dep}≤505°C exhibit MQW peaks and sharp fast interference fringes over a wide range of diffraction angles. This indicates low deterioration of vertical coherence of the MQW layers due to a lack of prominent closing edge segments (Lomer dislocations) in the MQW volume. In contrast, SL peaks and interference fringes in particular are considerably

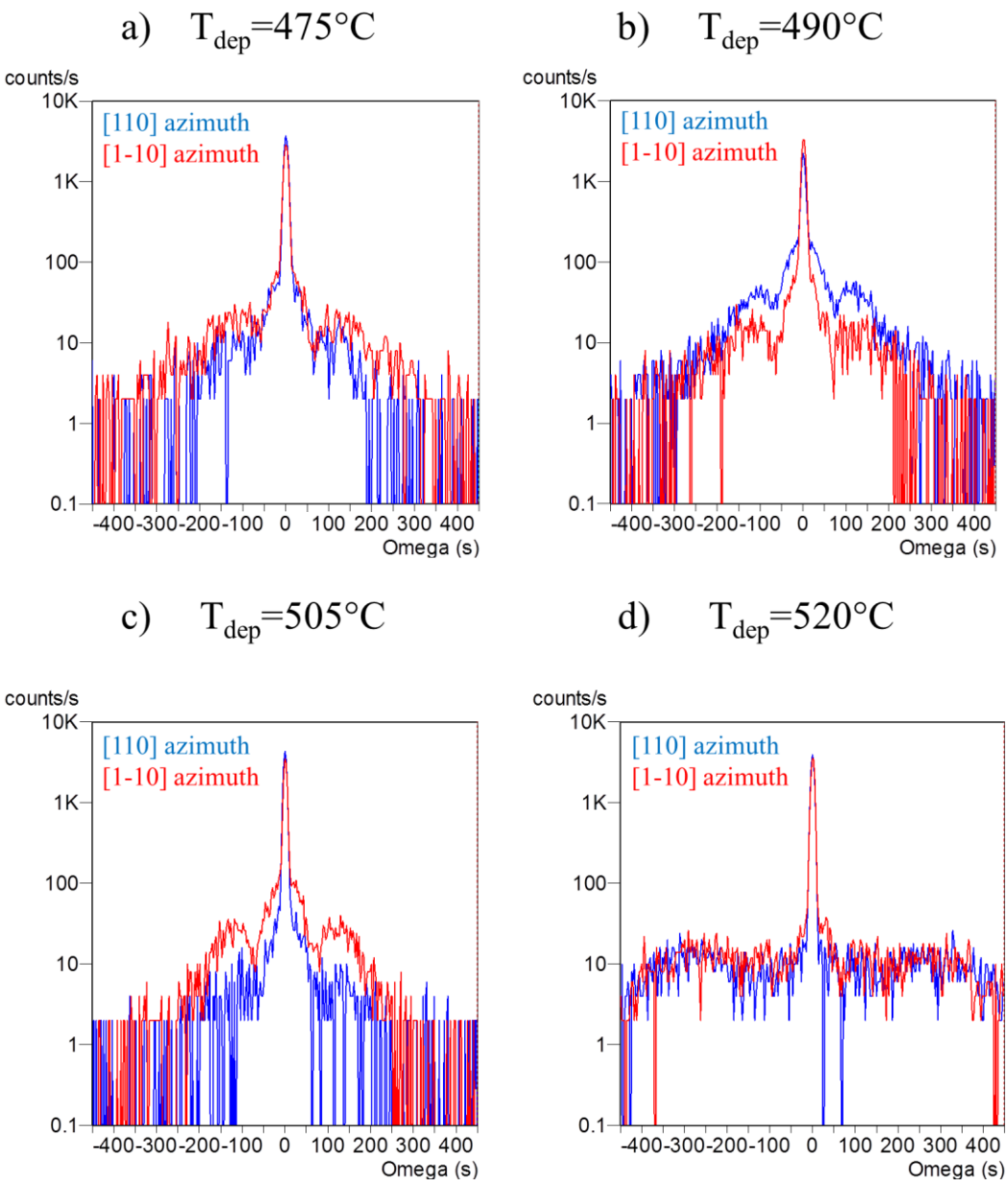

Fig. 20. TC ω RCs of All Samples 475°C ≤ T_{dep} ≤ 520°C.

diffused for the sample T_{dep}=520°C, as a result of reduced vertical coherence. Quantitative results were extracted from the FWHM of MQW peaks in triple crystal (TC) ω-2θ scans, see Equation (5) and Table 3. While the three samples grown at lower temperature exhibit similar vertical coherence lengths ~97 nm, the fourth sample reveals reduced vertical

Table 3. Structural Parameters of the MQW Layers Obtained from HR-XRD Measurements.

Sample ID	**G13-013**	**G13-009**	**G13-011**	**G13-007**
T_{dep} [°C]	**475**	**490**	**505**	**520**
T_{InGaAs}/T_{GaAs} [nm]	8/8.1	8.2/8	8/8.1	8.1/8
X_{In} [%]	20.8	20.5	20.6	18.5
FWHM TC ω-2θ [arc sec]	176	174	176	228
FWHM TC ω RC [arc sec]	12.2	11.2	9.4	10.1
$L_{vert.coh.}$ [nm]	97	98	97	75
$N_{primary\ DLs}$ [cm^{-2}]	$5.5 \cdot 10^5$	$4.3 \cdot 10^5$	$3.0 \cdot 10^5$	$3.7 \cdot 10^5$
$N_{secondary\ DLs}$ [cm^{-2}]	$2.7 \cdot 10^7$	$1.6 \cdot 10^7$	$1.0 \cdot 10^7$	$1.2 \cdot 10^7$
Relaxation [%]	0	0	0	<1

coherence ~75 nm. This is in line with the distinct observation of extended SL peaks and fast interference fringes. The maximal obtained coherence length exceeds the MQW structure thickness 80 nm, as FWHM and shape of TC RCs result from x-ray interference involving other layers. Hence coherence lengths might not exactly correspond to the physical thickness of a MQW structure.

Information about type, density, and spatial distribution of preferred crystalline defects were extracted from the shape and parameters of respective TC ω RCs. Fig. 20 depicts RCs collected on the -1SL peak (see Fig. 18), for two azimuthal directions [110] and [1-10]. The general appearance reveals a narrow coherent central peak as well as distinct shapes

and extents of diffuse scattering. The linewidth of the narrow coherent peak is used to estimate the density of primary 60° dislocation loops (DL). A trend of increasing primary DL density with decreasing deposition temperature can be extracted from T_{dep}=505°C on. The significance of this trend is, however, limited as each value lies within an estimated error range of the other respective densities. Pronounced interference wings (at $\Delta\omega\approx\pm150$ arc sec) in the diffuse scattering range for the structures $T_{dep}\leq505$°C suggest lateral ordering of secondary 60° dislocation loops in the volume. Their density can be estimated from the width of the base below the narrow coherent peaks. Like the primary DL density, the density of secondary DLs exhibits an increase with decreasing deposition temperature from T_{dep}=505°C on. Particular differences in pronunciation of interference wings and diffuse scattering base depending on the azimuthal angle can be observed for each sample, respectively. The RC for sample T_{dep}=505°C measured in [110] azimuth reveals the lowest amount of diffuse scattering among all curves. Crystal deterioration observes a minimum in this sample along the [110] direction. In contrast to pronounced interference wings, the RC of the structure T_{dep}=520°C shows a broad range of diffuse scattering contributions. Crystalline deteriorations are hence assigned to comparatively small defects with a more isotropic spatial distribution in the volume. The azimuthal anisotropy is lifted.

Symmetrical ω-$2\theta/\omega$ reciprocal space maps (RSM) collected around (004) GaAs diffraction spot are depicted in Fig. 21. The samples grown at the three lowest temperatures reveal narrow diffraction peaks elongated along the vertical diffraction vector. The peaks are connected by a streaky surface truncation rod as a result of high vertical coherence. In structure T_{dep}=475°C the surface truncation rod is slightly less pronounced, indicating inferior vertical coherence as compare to the other two structures. All RSMs exhibit areas

of diffuse scattering in the vicinity of the coherent scattering spots. Weakest diffuse scattering was found for T_{dep}=505°C with only faint scattering extending into lateral diffraction direction, as a result of high crystalline quality. RSMs visually confirmed the amount of diffuse scattering increases with reduced deposition temperature between T_{dep}=505°C and T_{dep}=475°C.

On the contrary, the symmetric RSM of structure T_{dep}=520°C does not reveal a pronounced surface truncation rod. The vertical coherence is considerably reduced when compared to all the other three structures. Besides, the graph shows extensive areas of diffuse scattering, indicating high crystalline deterioration with a broad range of length scales.

The extent of relaxation of initial elastic stress was inferred from asymmetrical ω-2θ/ω RSMs collected around the (224) GaAs diffraction spot, Fig. 22. All RSMs are composed of the coherent (224) GaAs spot (red bar) and a series of (224) SL peaks (black bar). Diffraction peaks appear clear and narrow for the structures T_{dep}=490°C and T_{dep}=505°C, or less intense (T_{dep}=475°C) and diffused (T_{dep}=520°C). Coinciding lateral positions for (224) GaAs spot and (224) InGaAs – SL spots visually confirm a lack of relaxation in the structures $T_{dep}\leq$505°C. The number of created secondary DLs did not suffice to initiate overall strain accommodation. In contrast, < 1% relaxation was observed in the sample T_{dep}=520°C, along with wide areas of diffuse scattering.

The evaluation of several HR-XRD experiments, namely DC and TC ω-2θ scans, TC ω RCs, and symmetrical as well as asymmetrical RSMs, reveals a coherent picture of crystalline quality and defect creation in four examined structures. Deposition at T_{dep}=505°C was identified as optimal temperature for epitaxial growth resulting in best

quality InGaAs layers with 20% In composition. Lower temperatures revealed a gradual increase in 60° primary and secondary DL density, and a decrease in lateral and vertical coherence. Lateral spatial ordering at these temperatures is contrasted by more isotropically distributed defects for the structure grown above the optimal T_{dep} found. Such high deposition temperature (T_{dep}=520°C) led to minimal vertical and lateral coherence, highest crystal deterioration among the investigated samples, and initial stress relaxation.

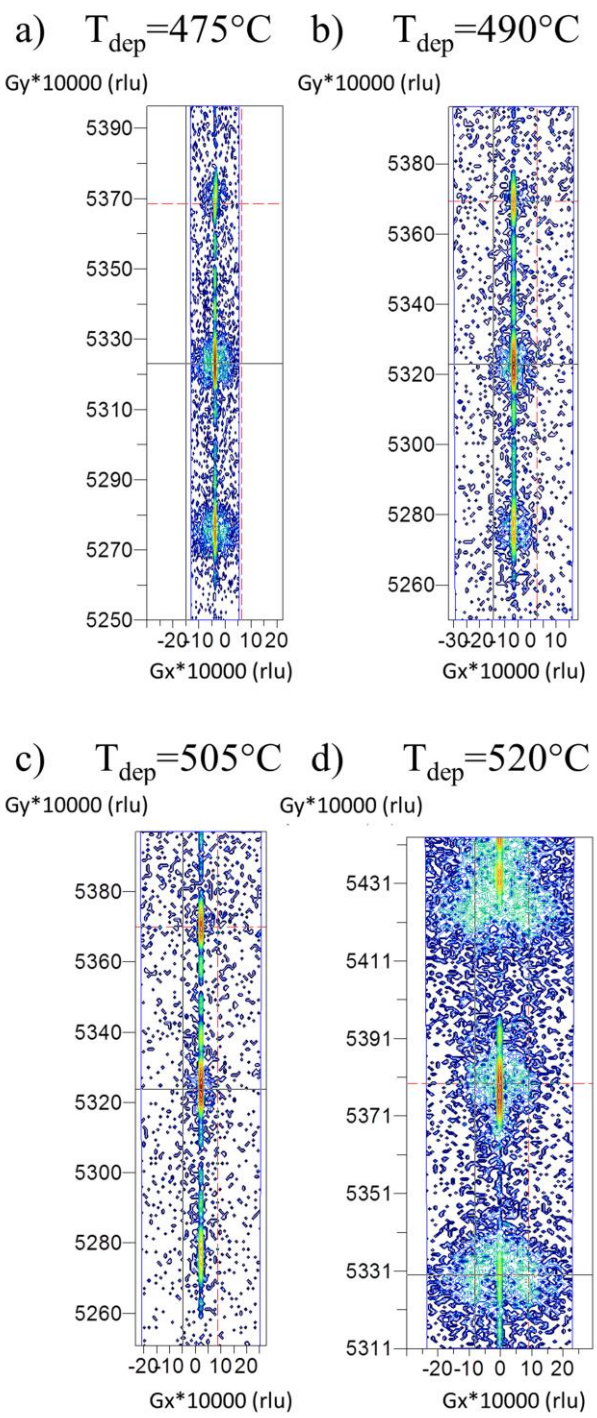

Fig. 21. Symmetrical Reciprocal Space Maps for All Samples 475°C ≤ T_{dep} ≤ 520°C Collected around the (004) 0 SL Spot of the MQW Structure. The 0SL Peak of the MQW Structure Is Indicated by the Red Horizontal Bar, While the -1SL Peak Is Located on the Black Horizontal Bar.

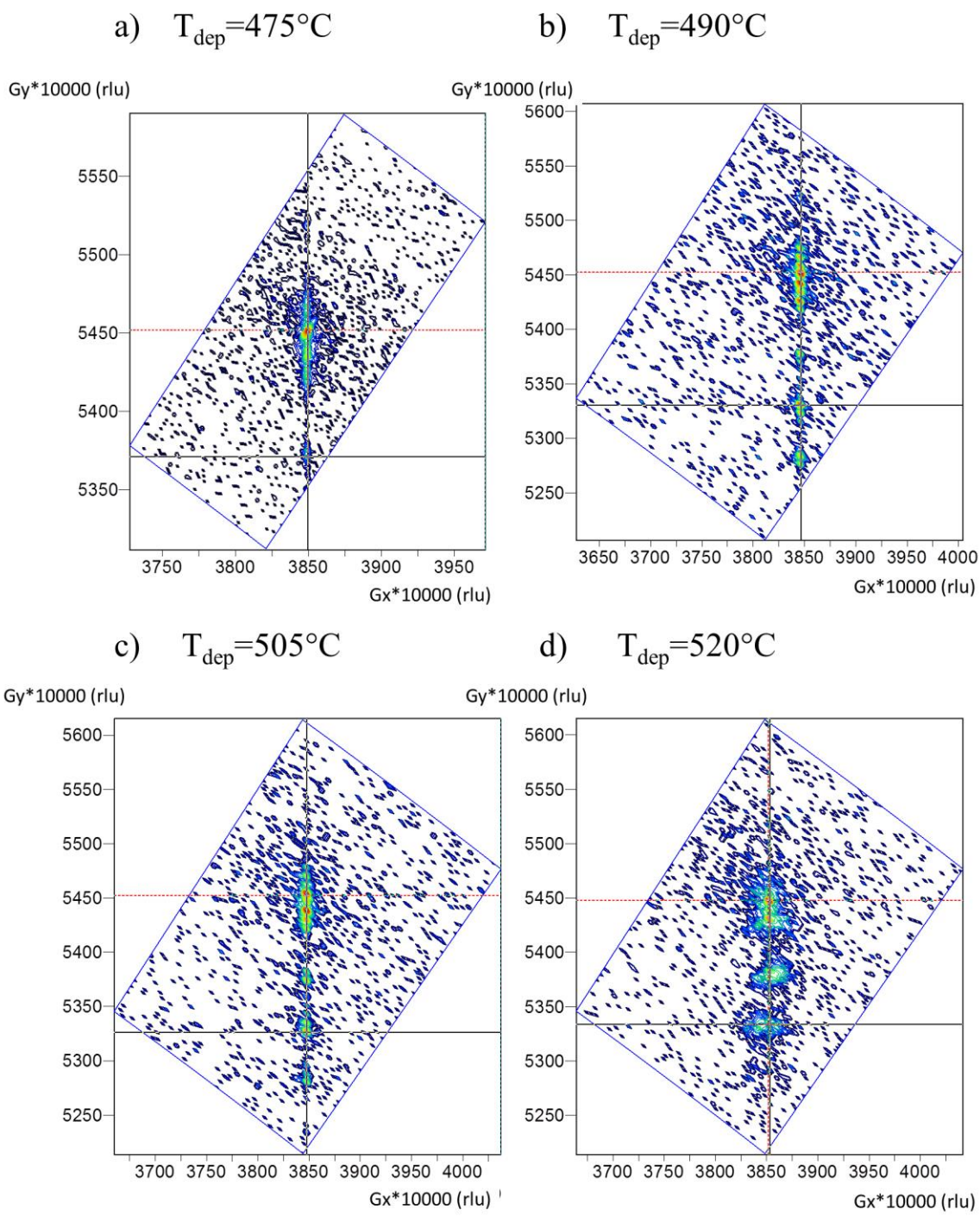

Fig. 22. Asymmetrical Reciprocal Space Maps for All Samples 475°C ≤ T_{dep} ≤ 520°C Collected around the (224) GaAs Diffraction. The (224) GaAs Diffraction Spot Is Indicated by the Red Horizontal Bar, While the (224) SL Peak of the MQW Structure Is Located on the Black Horizontal Bar.

5.2. Examination of Optical Properties

Optical properties were examined by means of photoluminescence spectroscopy as described in section 4.3.

Brightest luminescence was observed for the sample T_{dep}=505°C; its PL spectrum measured at 5 K is shown in Fig. 23. The spectrum is composed of a narrow (~8 meV) transition at ~1.323 eV, a slightly broader "peak 2" at about the same energy, and a broad (~28 meV) peak at ~1.308 eV. Measurements were carried out over the temperature range 5 – 300 K. The obtained spectra were decomposed into the three observed peaks via Gauß'ian curve fitting and the fit parameters extracted. This allowed to extract the temperature dependence of the three individual transitions, Fig. 24. The narrow peak follows neatly the simulated transition energies (Varshni dependence [55]) for a MQW structure with proper dimensions and composition, as simulated by self-consistent

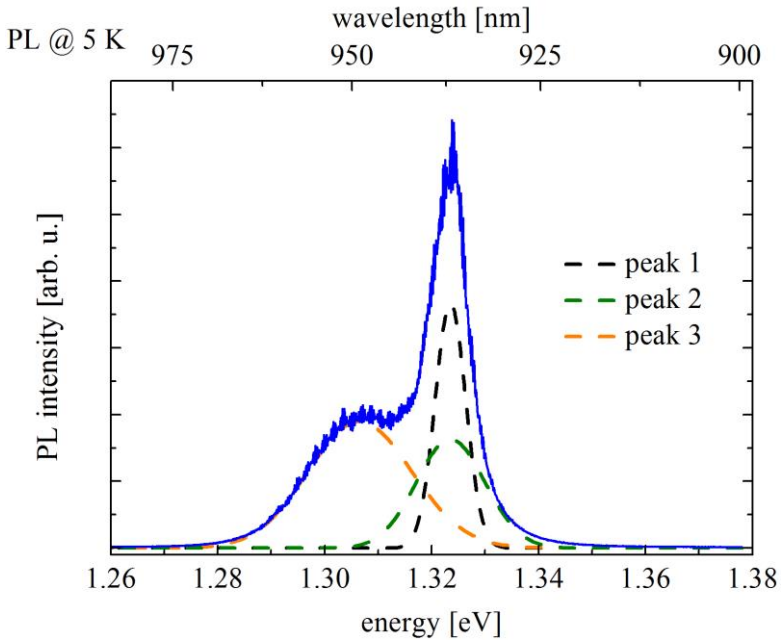

Fig. 23. Photoluminescence Spectrum of the Sample T_{dep}=505°C Measured at 5 K Ambient Temperature. A Deconvolution of the Curve into Three Peaks Allows the Individual Temperature Behavior to Be Studied.

Schrödinger-Poisson calculations (see section 3.3.5). The positions of "peak 1" and "peak 2" coincide at low temperature. Both peaks experience red shift with rising temperature, however, with an increasing energy difference between these two peaks. These transitions can be ascribed to carrier confinement states in the MQW, while the peak separation trend accounts for band filling as the temperature goes up. The increasing occupation of higher energy states with reference to the band edge at elevated temperature, band filling, is a result of a spreading Fermi distribution function. The indicated "peak 3" stays rather constant over the whole temperature range, indicating a carrier state with a temperature insensitive, constant energy. This feature and the high line-width suggest a defect-related origin.

Excitation power dependent PL was performed on those samples (grown at $T_{dep} \leq 505°C$) with a Varshni-like temperature dependence of the MQW transition energy. Spectra at four particular excitation powers are depicted in Fig. 25. Two structures $T_{dep}=475°C$ and

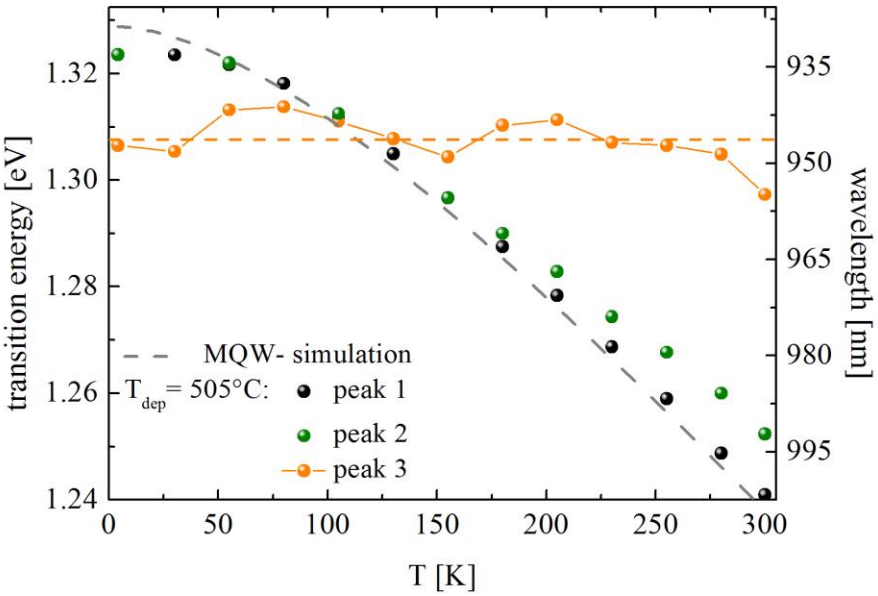

Fig. 24. Temperature Evolution of the PL Transition Energies for the Three Peaks Indicated in Fig. 23. The MQW Peak (Black Dots) Follows Neatly the Calculated Transition Energy Obtained from Schrödinger-Poisson Simulations (Dashed Line).

T_{dep}=490°C reveal a single prominent transition with weak energy dependence on excitation power (~2 meV blueshift for depicted spectra) and weak sub-bandgap luminescence. The energetic position deviates by 23 meV and 18 meV from the simulated MQW transition value for the samples T_{dep}=475°C and T_{dep}=490°C, respectively. In both cases the linewidth is about 10 meV (~7 nm). In contrast, the structure T_{dep}=505°C reveals both the MQW state and prominent sub-bandgap transitions. At low excitation the intensity of the sub-bandgap luminescence exceeds the one of the MQW peak, whereas its relative intensity decreases with rising pumping level. This indicates a saturation of these optically active sub-bandgap states with increasing generated carrier density, whereupon the radiative recombination via the MQW states becomes relatively stronger. The sub-bandgap transition was already found in the temperature dependent PL (compare Fig. 23 with adequate excitation power 1 mW - red in Fig. 25). The linewidth of the MQW transition is ~10-12 meV (~9 nm). The narrow linewidths of all three MQW structures indicate high material quality[7].

[7] Compare to 6.3 meV in [13]: 5K spectrum of InGaAs-single quantum well, X_{In}~26%, thickness: 6.8 nm

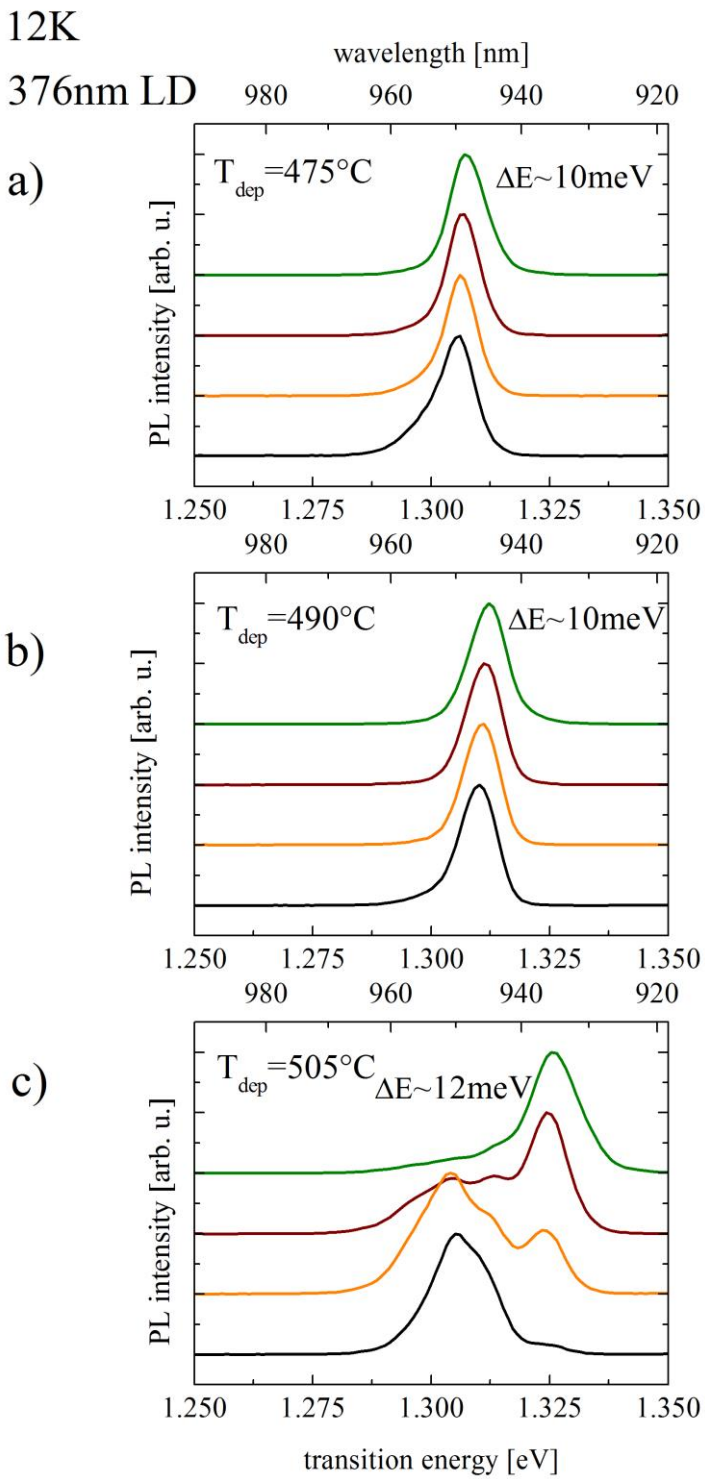

Fig. 25. PL Spectra (12 K) with Increasing Excitation Power (from Black to Green Curve). Spectra of Samples T_{dep}<505°C (A and B) Show Weak Sub-Bandgap Luminescence, While Several Sub-Bandgap Transitions (Compare Fig. 23) Appear for T_{dep}=505°C (C). Spectra are Normalized and Stacked with Increasing Excitation Power (0.07, 0.4, 1, 7.7 mW).

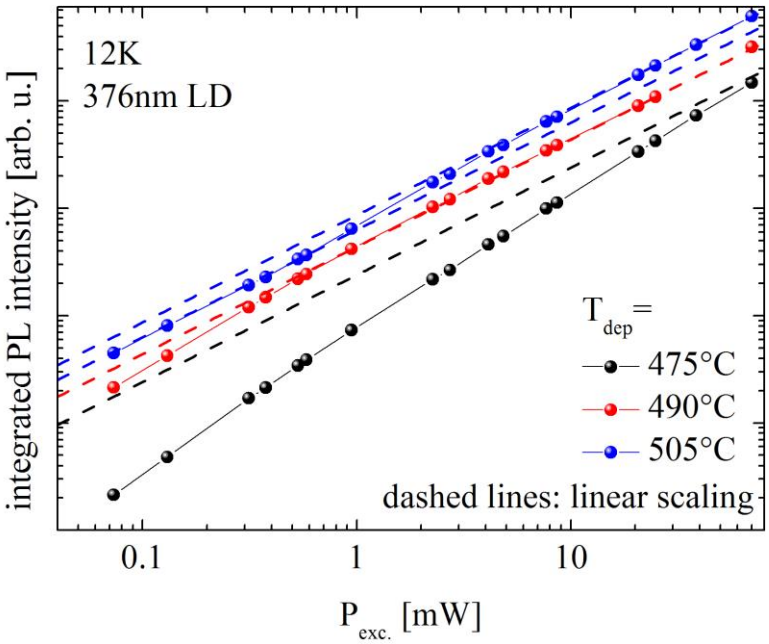

Fig. 26. Integrated PL Intensity Over Three Orders of Magnitude in Excitation Power Measured at 12 K. Sample T_{dep}=505°C Reveals Brightest Luminescence. The Gradation in Scaling Exponent among the Three Samples Indicates Distinct Strengths of Non-Radiative SRH Recombination.

Integration of the obtained intensity spectra over the entire wavelength range resulted in the excitation power dependence depicted in Fig. 26. The dashed lines in this log-log plot indicate linear scaling. Distinct trends in scaling exponent can be extracted. The structure T_{dep}=475°C reveals hyper-linear behavior over the entire excitation range covered, whereas T_{dep}=490°C transitions from a hyper-linear dependence into a linear trend. The sample with brightest luminescence T_{dep}=505°C shows continuous linear scaling, however with a change in slope at about 1 mW excitation. This behavior can be compared to the prediction of the model proposed in section 3.3.4. It predicts a transition of the PL intensity vs. excitation power curve from a square into a linear dependence with increasing pumping level. Stronger SRH-recombination requires higher laser power P_{exc} to reach the linear PL-intensity regime. The change in scaling exponent $k = \mathrm{d}\log(I_{\mathrm{PL}})/\mathrm{d}\log(P_{\mathrm{exc}})$ of the

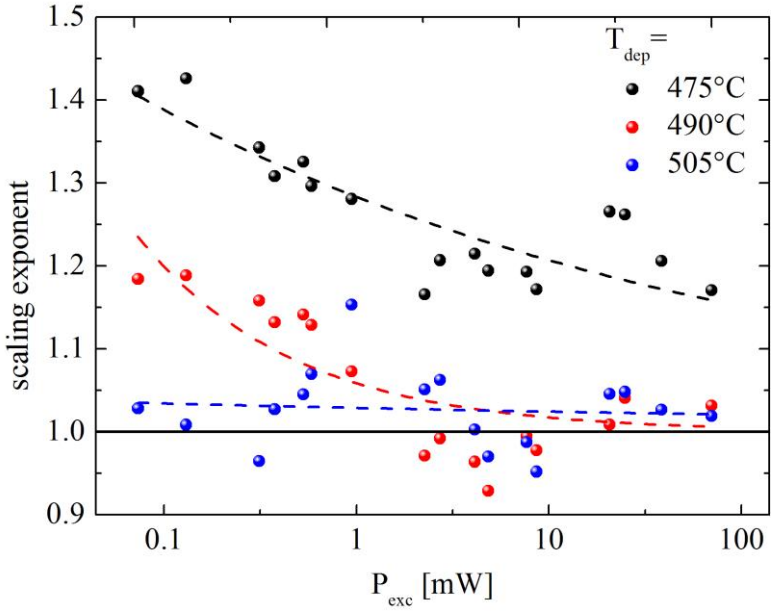

Fig. 27. Whereas the Structures T_{dep}=505°C and T_{dep}=490°C Transition into the Linear Regime, the Sample T_{dep}=475°C Reaches the Scaling Exponent 1.2.

experimental data is shown in Fig. 27. With the proposed model at hand, the scaling exponent dependence can be interpreted as follows. For the sample T_{dep}=475°C the non-radiative recombination sites are not saturated over the covered excitation range, unlike sample T_{dep}=490°C in which the SRH trap-states are finally saturated, whereupon the PL intensity scales linearly. In this picture, sample T_{dep}=505°C has the least trap states as the PL intensity scales continuously linearly. The transition into this linear regime is hence likely to appear at lower excitation powers than used. The intensity dependence for this sample does, however, change its slope (scaling exponent 1.16 at 1 mW) when the PL spectrum switches from the sub-bandgap luminescence to the MQW transition as the main feature (see Fig. 25c).

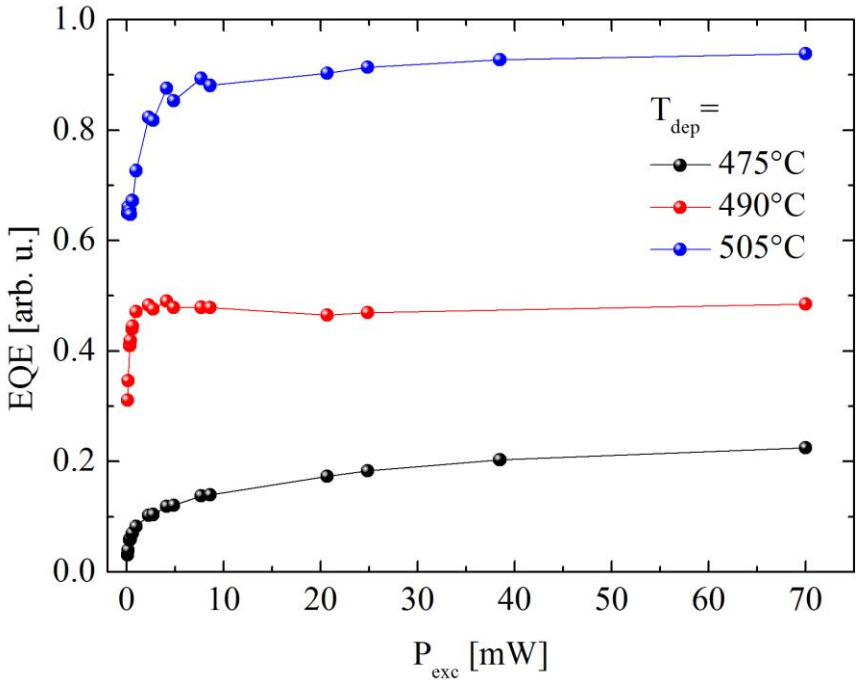

Fig. 28. The Shape of the EQE Curves Indicates That Auger Recombination Is Negligible over the Covered Excitation Power Range, If Compared to Fig. 11 (Inset). Even at Highest Pumping Level the MQW Emission Efficiency Does Not Droop.

The applied power dependent PL model assumed Auger-recombination to be negligible. That this requirement is fulfilled for the experimental data is confirmed by the plot (Fig. 28) of the external quantum efficiency EQE=IQE$\cdot \eta_{\mathrm{extr}} \propto I_{\mathrm{PL}}/P_{\mathrm{exc}}$, which is proportional to the internal quantum efficiency (IQE) introduced in section 3.3.4 (η_{extr} photon extraction efficiency).

The excitation power dependent PL experiment reveals continuously increasing non-radiative recombination site density if the deposition temperature is decreased from 505°C to 475°C.

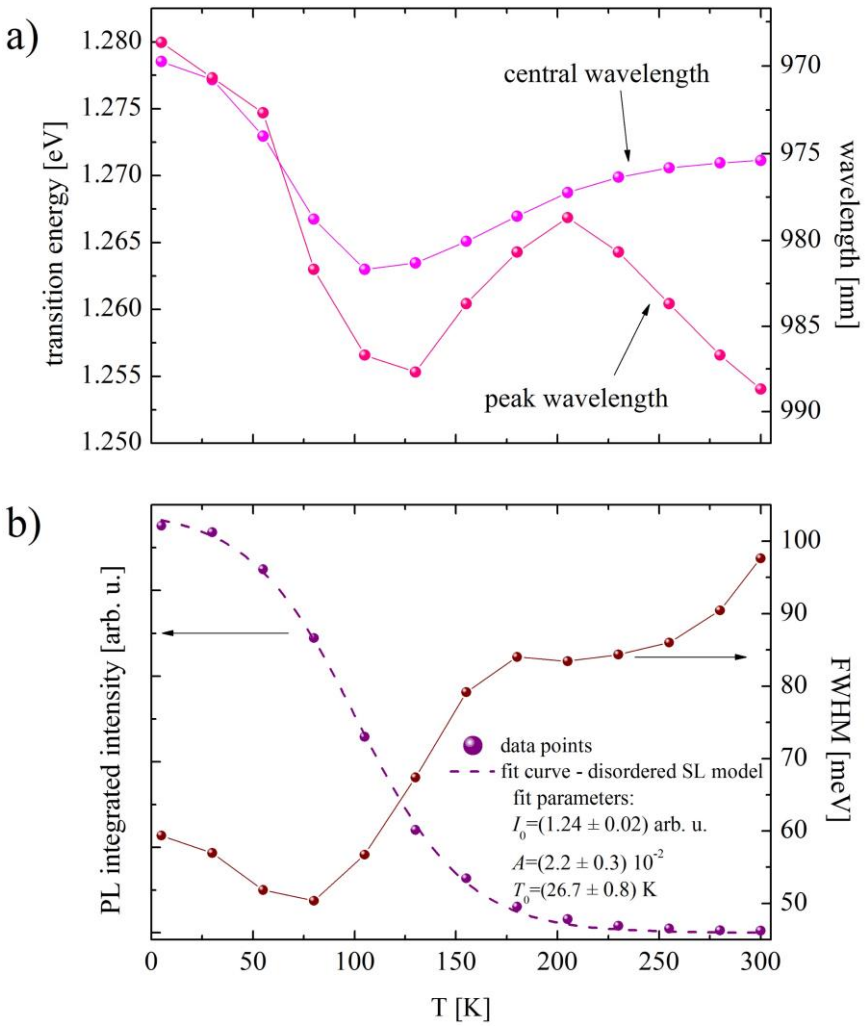

Fig. 29. a) Temperature Dependence of Central and Peak PL Transition Energy of the Sample T_{dep}=520°C. B) Along with Linewidth and Integrated PL Intensity Behavior, the Features Suggest the Presence of Random Band Edge Fluctuations in the Sample.

Unlike the samples T_{dep}≤505°C, which revealed a Varshni behavior of the temperature dependent PL transition energy, structure T_{dep}=520°C shows a different characteristic. Fig. 29a depicts the PL transition energy between 5 and 300 K ambient temperature. In contrast to a continuously decreasing energy, the obtained curve reveals non-monotonous behavior with rising temperature. A decrease in energy between 5 and ~110 K, is followed by an increasing trend. While the peak transition energy exhibits a local maximum at ~200K and a decrease beyond, the central energy saturates beyond its minimum at ~110 K. Central

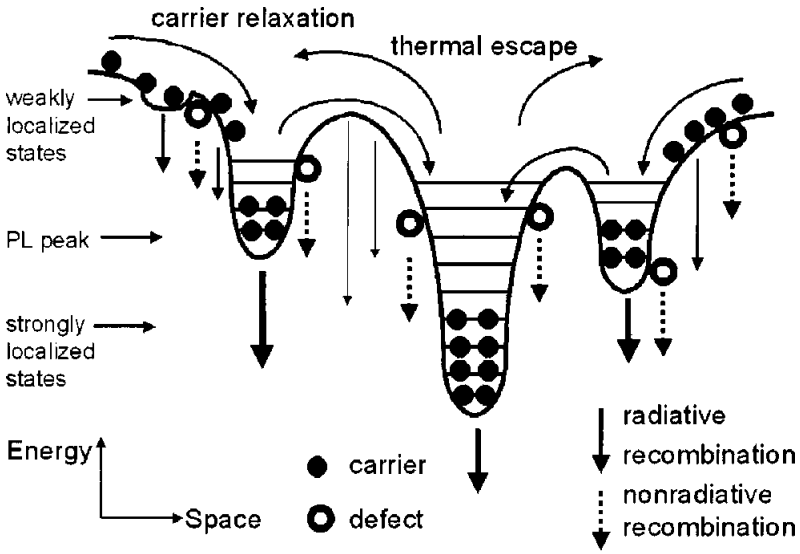

Fig. 30. Illustration of How Carrier Localization in Local Energy Minima May Influence Temperature Dependence of PL Transition Energy and Linewidth. [56]

and peak energy reveal similar values below 80 K. The difference between those energy values does not increase monotonously, as expected from band filling process, but instead exhibits a local minimum at ~200 K. The temperature dependent PL energy trend appears detached from the simulated Varshni dependence (Fig. 24).

The PL linewidth (Fig. 29b) is even at 5 K comparatively high (~60 meV). Increasing ambient temperature first leads to a decrease in linewidth until ~80 K and is then followed by increasing values. While the linewidth exhibits a nearly constant value between 180 and 230 K, it increases again beyond.

Both, the S-shape behavior of the PL transition energy and the non-monotonous linewidth dependence suggest the presence of random band edge fluctuations, which lead to localization of generated carriers in local energy minima. This mechanism of carrier localization in local energy minima was previously described in amorphous structures, disordered superlattices [57], and InGaN QWs with composition fluctuations [56, 58]. The

escape of carriers from local minima and their redistribution is a temperature activated process (Fig. 30), which results in the shown characteristic features [58]. The temperature dependence of the integrated PL intensity I_{PL} has been described by [57, 58]

$$I_{PL} = \frac{I_0}{1 + t\exp(T/T_0)} \tag{9}$$

where T_0 the characteristic temperature corresponding to the energy depth of localized states from a mobility edge, t is the tunneling factor and I_0 is the luminescence intensity in the low-temperature limit. This formula has been fitted to the experimental data as shown in Fig. 29b. The fit resulted in low statistical errors between 1 and 14% and high correlation indicated by a coefficient of determination R^2 of 0.9993. The good fit with the model proposed for carrier localization stresses the previously suggested random band edge fluctuations in sample T_{dep}=520°C.

The evaluation of several PL experiments, namely temperature dependent and excitation power dependent PL measurements reveals a coherent picture of the optical properties and defect creation in four examined structures. Deposition at T_{dep}=505°C was identified as optimal temperature for epitaxial growth resulting in best optical properties for InGaAs layers with 20% In composition. Lower temperatures revealed a gradual increase in non-radiative recombination strength. Varshni-like transition energy dependence for these deposition temperatures is contrasted by S-shape behavior at elevated deposition temperature indicating localization of generated carriers in local energy minima. Such high deposition temperature (T_{dep}=520°C) led to random band edge fluctuations, most likely related to InGaAs decomposition.

5.3. Correlation of Structural and Optical Properties with Growth Conditions

The deposition temperature T_{dep} was chosen as the variable growth parameter in this study. Deposition temperature is a major determinant of the mobility of atoms and molecules on the growth surface. In the experiment, the temperature range between 475°C and 520°C was covered. For temperatures 475°C$\leq T_{dep} \leq$505°C the major crystal deterioration was identified as primary and secondary 60° dislocation loops (DL), preceded by creation of point defects and their accumulation in pre-dislocation clusters. Creation of these defects did not suffice to accommodate the initial elastic strain resultant from the pseudomorphic growth of InGaAs on GaAs. In this temperature range, deposition temperature reduction resulted in both increased non-radiative SRH recombination and increased DL density. This correlation might be explained in two limiting ways:

On the one hand, point defects can create energy states in the band gap and act as non-radiative recombination sites. Consequently, higher trap state concentrations result in stronger SRH recombination. On the other hand, point defects and their clusters are the prerequisite for the creation of dislocations loops. In this reading, the trend of increasing DL density is correlated with the presence of its pre-stage, the point defects.

Conversely, dislocation loops are perturbations in a periodic crystal structure. As such disruptions, they introduce energy states into the band gap, by quantum mechanical principles. In a local picture, dislocation cores provide dangling bonds which may represent energy states in the band gap. In this reading, the trend of increasing SRH recombination is a result of increasing DL density. Neither one of these two extreme cases is an exact way

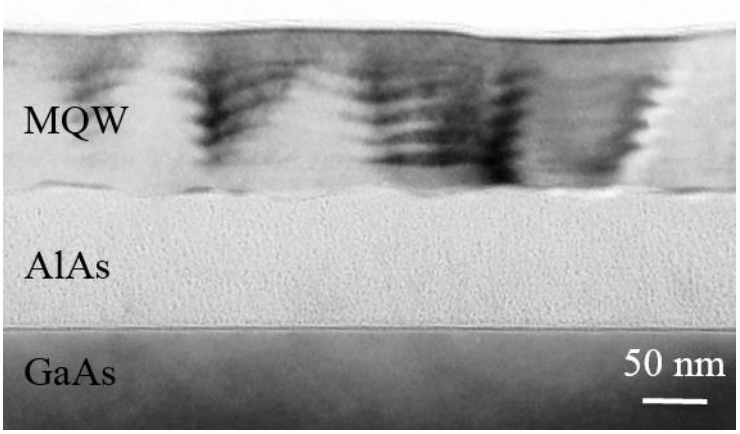

Fig. 31. Cross-section TEM of the ×5-MQW Structure Grown at T_{dep}=520°C as Illustration of Lateral Layer Thickness Modulations as a Result of Elevated Deposition Temperature and Indium Decomposition.

to describe the found correlation between DL density and SRH recombination strength. A mixture of both relationships may be the most appropriate description instead.

Surpassing the deposition temperature T_{dep}=505°C, identified as best value for the growth of $In_{0.2}Ga_{0.8}As$/GaAs MQWs, resulted in prominent deviations from both optimal crystalline and optical properties. Major crystalline defects were found to be of comparatively small spatial extent with isotropic distribution. Most likely In precipitates or clusters account for these deteriorations. This expresses instability of the InGaAs compound at elevated temperatures. In addition to that, elevated deposition temperature did not result in smooth interfaces but in layer thickness undulations instead. The cross-section transmission electron micrograph (TEM, Fig. 31) [8] shows lateral thickness modulations with a period of ~100 nm. This type of deterioration was attributed to the comparatively high deposition temperature used. *Shilkrot et al.* [59] present a theoretical stability analysis for epitaxial growth of strained-layer superlattices. Their model predicts

[8] Transmission electron microscopy was generously performed by Dr. David J. Smith, Department of Physics, Arizona State University, Tempe, AZ 85287, USA

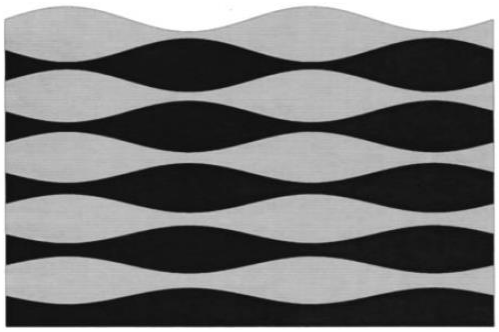

Fig. 32. Multilayer Film Morphology of an Out-Of-Phase Instability. [59]

a change from stable growth resulting in flat interfaces, to a regime in which the surface is unstable with respect to the growth of perturbations once a critical surface diffusivity is exceeded. Fig. 32 depicts an illustration of the multilayer film morphology the authors predict for elevated surface diffusivity. Such modulations in the MQW layers cause local fluctuations in the averaged composition.

The two observed instabilities, namely the InGaAs decomposition and structural instability with respect to layer undulations, represent origins of modulations in the local band edge in the MQW volume. Band edge fluctuations are the cause for the localization of charge carriers in local energy minima. The occurrence of the carrier localization mechanism was observed in the structure T_{dep}=520°C as a prominent feature in the optical properties. The observed optical properties are hence a direct result of the structural and crystalline features.

InGaAs/GaAs MQW structures reveal correlation between their crystal quality and optical properties with used MBE deposition temperature in the range between 475°C and 520°C.

CHAPTER 6

CONCLUSIONS

In this thesis, the epitaxial growth of InGaAs/GaAs MQW structures at the initial stage of defect creation was studied. The work correlates crystalline and optical properties of grown structures with the deposition temperature used during MBE growth.

Suitable techniques and metrics for the examination of crystalline and optical properties were chosen and the evaluation of experimental data established. In particular, a model for the analysis of the strength of non-radiative SRH recombination on the basis of excitation power dependent PL spectra was proposed. The model assumes charge carriers to be spatially confined in an active region upon generation by an external light source. The dependence of the luminescence intensity is related to the laser power in an excitation limit, in which only SRH and radiative recombination need to be considered. The transition from square into linear scaling is pivotal in the assessment of non-radiative SRH recombination strength.

Four InGaAs/GaAs MQW structures with 20% In composition were epitaxially grown at deposition temperatures between 475°C and 520°C. The grown samples were characterized by means of HR-XRD and PL. Deposition at T_{dep}=505°C was identified as optimal value for the growth at 20% In composition. For the temperature range 475°C $\leq T_{dep} \leq$505°C, primary and secondary 60° dislocation loops were identified as main crystalline deterioration. The density of both kinds of mixed-type dislocations increased continuously with decreasing deposition temperature. Likewise non-radiative SRH recombination became more dominant as growth temperature was reduced. Hence, crystalline and optical properties exhibit a correlation with the used growth condition.

Exceeding the optimal value T_{dep}=505°C revealed two kinds of instabilities at T_{dep}=520°C. Material instability led to InGaAs decomposition and structural instability resulted in layer thickness undulations. Both features represent causes for fluctuations of the local bandgap, which may affect optical properties. The experimental optical analysis suggests the localization of charge carriers in local energy minima. These local energy minima are hence assumed to result from the fluctuations in the local bandgap. The found material and morphology instabilities can thus be directly correlated with the optical properties.

The experiments on growth and characterization of InGaAs/GaAs MQWs reveal an optimal deposition temperature range for each In composition. Obtained structures are characterized by high crystal perfection and best optical response.

For device and growth process design, it is of special importance to consider correlations between physical properties, such as the optical response, and crystal perfection as dependent on growth conditions. Suboptimal growth conditions can easily deteriorate material quality and degrade final device performance. The results allow to optimize structure design and epitaxial growth of MQWs for various device applications.

REFERENCES

[1] K. Lasswitz. *Wirklichkeit – Beiträge zum Weltverständnis.* Verlag von Emil Feber, 1900.

[2] Z.I. Alferov. Nobel Lecture: The double heterostructure concept and its applications in physics, electronics, and technology. *Reviews of Modern Physics* 73(3):767-782, 2001.

[3] H. Kroemer. Theory of wide-gap emitter for transistors. *Proceedings of the IRE* 45(11):1535-5137, 1957.

[4] H. Kroemer. A proposed class of hetero-junction injection lasers. *Proceedings of the IEEE* 51(12):1782-1783, 1963.

[5] R. Dingle, W. Wiegmann, C.H. Henry. Quantum states of confined carriers in very thin $Al_xGa_{1-x}As$-GaAs-$Al_xGa_{1-x}As$ heterostructures. *Physical Review Letters* 33(14):827-830, 1974.

[6] H. Kroemer. Noble Lecture: Quasielectric fields and band offsets: teaching electrons new tricks. *Reviews of Modern Physics* 73(3):783-793, 2001.

[7] M. Quillec, L. Goldstein, G. Le Roux, J. Burgeat, J. Primot. Growth conditions and characterization of InGaAs/GaAs strained layers superlattices. *Journal of Applied Physics* 55(8):2904-2909, 1984.

[8] B. Grandidier, H. Chen, R.M. Feenstra, D.T. McInturff, P.W. Juodawlkis, S.E. Ralph. Scanning tunneling microscopy and spectroscopy of arsenic antisites in low temperature grown InGaAs. *Applied Physics Letters* 74(10):1439-1441, 1999.

[9] J.F. Klem, W.S. Fu, P.L. Gourley, E.D. Jones, T.M. Brennan, J.A. Lott. Role of substrate threading dislocation density in relaxation of highly strained InGaAs/GaAs quantum well structures. *Applied Physics Letters* 56(14):1350-1352, 1990.

[10] D.C. Bertolet, J.K. Hsu, K.M. Lau, E.S. Koteles, D. Owens. Exciton photoluminescence linewidths in very narrow AlGaAs/GaAs and GaAs/InGaAs quantum wells. *Journal of Applied Physics* 64(11):6562-6564, 1988.

[11] G.W. Pickrell, K.L. Chang, J.H. Epple, K.Y. Cheng, K.C. Hsieh. Growth of low-defect density $In_{0.25}Ga_{0.75}As$ on GaAs by molecular beam epitaxy. *Journal of Vacuum Science and Technology B* 18(6):2611-2614, 2000.

[12] A. Madhukar, K.C. Rajkumar, L. Chen, S. Guha, K. Kaviani, R. Kapre. Realization of low defect density, ultrathick, strained InGaAs/GaAs multiple quantum well structures via growth on patterned GaAs(100) substrates. *Applied Physics Letters* 57(19):2007-2009, 1990.

[13] R.L.S. Devine. PL characterization of InGaAs/GaAs QW structures. *Semiconductor Science and Technology* 3:1171-1176, 1988.

[14] J.W. Matthews, A.E. Blakeslee. Defects in epitaxial layers III. Preparation of almost perfect multilayers. *Journal of Crystal Growth* 32(2):265-273, 1976.

[15] B. Elman, E.S. Koteles, P. Melman, C. Jagannath, J. Lee, D. Dugger. In situ measurements of critical layer thickness and optical studies of InGaAs quantum wells grown on GaAs substrates. *Applied Physics Letters* 55(16):1659-1661, 1989.

[16] E.A. Fitzgerald, D.G. Ast, P.D. Kirchner, G.D. Pettit, J.M. Woodall. Structure and recombination in InGaAs/GaAs heterostructures. *Journal of Applied Physics* 63(3):693-703, 1988.

[17] J. Zou, D.J.H. Cockayne. Lomer-Cottrell misfit dislocations in [001] $In_{0.2}Ga_{0.8}As$/GaAs single heterostructures. *Applied Physics Letters* 69(8):1083-1085, 1996.

[18] J.W. Matthews, A.E. Blakeslee. Defects in epitaxial multilayers I. Misfit dislocations. *Journal of Crystal Growth* 27:118-125, 1974.

[19] K.J. Beernink, P.K. York, J.J. Coleman, R.G. Waters, J. Kim, C.M. Wayman. Characterization of InGaAs-GaAs strained-layer lasers with quantum wells near critical thickness. *Applied Physics Letters* 55(21):2167-2169, 1989.

[20] J.F. Geisz, S. Kurtz, M.W. Wanlass, J.S. Ward, A. Duda, D.J. Friedman, J.M. Olson, W.E. McMahon, T.E. Moriarty, J.T. Kiehl. High-efficiency GaInP/GaAs/InGaAs triple-junction solar cells grown inverted with a metamorphic bottom junction. *Applied Physics Letters* 91:23502-1 – 23502-3, 2007.

[21] K. Barnham, I. Ballard, J. Connolly, N. Ekins-Daukes, B. Kluftinger, J. Nelson, C. Rohr. Quantum Well Solar Cells. *Physica E* 14:27-36, 2002.

[22] C.B. Honsberg, S.P. Bremner, R. Corkish. Design trade-offs and rules for multiplex energy level solar cells. *Physica E* 14:136-141, 2002.

[23] A. Freundlich, G.K. Vijaya, A. Mehrotra. Superlattice intermediate band solar cell with resonant upper-conduction-band assisted photo-absorption and carrier extraction. *Proceedings of* 39th *IEEE PVSC* 1635-1638, 2013.

[24] C.Z. Ning. Semiconductor nanolasers. *Physica Status Solidi B* 247(4):774-788, 2010.

[25] M.T. Hill. Status and prospects for metallic and plasmonic nano-lasers. *Journal of the Optical Society of America B* 27(11):B36-B44, 2010.

[26] K. Ding, Z.C. Liu, L.J. Yin, M.T. Hill, M.J.H. Marell, P.J. van Veldhoven, R. Nöetzel, C.Z. Ning. Room-temperature continuous wave lasing in deep-subwavelength metallic cavities under electrical injection. *Physical Review B* 85:041301-1 – 041301-5, 2012.

[27] K. Ploog. Molecular beam epitaxy of III-V compounds: Technology and growth process. *Annual Review of Materials Research* 11:171-210, 1981.

[28] H. Ibach, H. Lüth. *Solid State Physics.* Springer, 2003.

[29] M.A. Herman, W. Richter, H. Sitter. *Epitaxy: Physical principles and technical implementation.* Springer, 2004.

[30] B. Hillebrands. "Molecular beam epitaxy – Technische Universität Kaiserslautern". *http://www.physik.uni-kl.de/hillebrands/research/methods/molecular-beam-epitaxy/* accessed July 2014.

[31] H. Föll, B. Koblesen. *Agglomerate von Zwischengitteratomen (Swirl-Defekte) in Silizium – ihre Bedeutung für Grundlagenforschung und Technologie*. Jahrbuch der Akademie der Wissenschaften in Göttingen, Vandenhoeck & Ruprecht, 1976.

[32] N. Faleev, N. Sustersic, N. Bhargava, J. Kolodzey, A. Yu. Kazimirov, C. Honsberg. Structural investigations of SiGe epitaxial layers grown by molecular beam epitaxy on Si(001) and Ge(001) substrates: I-High resolution x-ray diffraction and x-ray topography. *Journal of Crystal Growth* 365:44-53, 2013.

[33] N. Faleev, N. Sustersic, N. Bhargava, J. Kolodzey, S. Magonov, D.J. Smith, C. Honsberg. Structural investigations of SiGe epitaxial layers grown by molecular beam epitaxy on Si(001) and Ge(001) substrates: II-Transmission electron microscopy and atomic force microscopy. *Journal of Crystal Growth* 365:35-43, 2013.

[34] S.P. Bremner, K.Y. Ban, N.N. Faleev, C.B. Honsberg, D.J. Smith. Impact of stress relaxation in GaAsSb cladding layers on quantum dot creation in InAs/GaAsSb structures grown on GaAs (001). *Journal of Applied Physics* 114(10):103511-1 – 103511-9, 2013.

[35] N.W. Ashcroft, N.D. Mermin. *Solid State Physics.* Brooks/Cole, 1976.

[36] U. Pitsch, V. Holy, T. Baumbach. *High resolution x-ray scattering from thin films and multilayers.* Springer, 1999.

[37] C. Suryanarayana, M. Grant Norton. *X-ray diffraction: A practical approach.* Plenum Press, 1998.

[38] P.F. Fewster. X-ray diffraction from low-dimensional structures. *Semiconductor Science and Technology* 8(11):1915-1934, 1993.

[39] PANalytical manual. *Epitaxy and Smoothfit – Software for the analysis of thin layers.* 2009.

[40] J.E. Ayers. The measurement of threading dislocation densities in semiconductor crystals by x-ray diffraction. *Journal of Crystal Growth* 135:71-77, 1994.

[41] V.M. Kaganer, R. Köhler, M. Schmidtbauer, R. Opitz, B. Jenichen. X-ray diffraction peaks due to misfit dislocations in heteroepitaxial structures. *Physical Review B* 55(3):1793-1810, 1997.

[42] Ioffe Institute. "Band structure and carrier concentration of Gallium Arsenide (GaAs)". *http://www.ioffe.ru/SVA/NSM/Semicond/GaAs/bandstr.html* accessed May 2014.

[43] W. Shockley, W.T. Read. Statistics of the recombination of holes and electrons. *Physical Review* 87(5):835-842, 1952.

[44] R.N. Hall. Electron-Hole Recombination in Germanium. *Physical Review* 87(2):387, 1952.

[45] E. Rosencher, B. Vinter, P.G. Piva. *Optoelectronics.* Cambridge University Press, 2002.

[46] L. Meitner. Über die β-Strahl-Spektra und ihren Zusammenhang mit der γ-Strahlung. *Zeitschrift für Physik A. Hadrons and Nuclei* 11:35-54, 1922.

[47] Z. Garbuzov. Reradiation effects, lifetimes and probabilities of band-to-band transitions in direct A_3B_5 compounds of GaAs type. *Journal of Luminescence* 27:109-112, 1982.

[48] K.A. Bulashevich, S. Yu. Karpov. Is Auger recombination responsible for the efficiency rollover in III-nitride light-emitting diodes? *Physica Status Solidi C* 5(6):2066-2069, 2008.

[49] P. Dirac. The quantum theory of the emission and absorption of radiation. *Proceedings of the Royal Society of London A* 114:243-265, 1927.

[50] C. Weisbuch, B. Vinter. *Quantum semiconductor structures – fundamentals and applications.* Academic Press, 1991.

[51] D.L. Smith, C. Mailhiot. Theory of semiconductor superlattice electronic structure. *Reviews of Modern Physics* 62(1):173-234, 1990.

[52] P. Yu, M. Cardona. *Fundamentals of semiconductors: physics and materials properties*. 3rd edition, Springer, 2001.

[53] S. Birner. "nextnano3 – next generation 3D nanodevice simulator". *http://www.nextnano.com/nextnano3/index.htm* accessed February 2013.

[54] B. Galler. *Ladungsträger-Rekombination und -Transport in InGaN-basierenden Leuchtdioden.* PhD thesis, Freiburg University, 2014.

[55] Y.P. Varshni. Temperature dependence of the energy gap in semiconductors. *Physica* 34(1):149-154, 1967.

[56] S.W. Feng, Y.C. Cheng, Y.Y. Chung, C. Yang, Y.S. Lin, C. Hsu, K.J. Ma, J.I. Chyi. Impact of localized states on the recombination dynamics in InGaN/GaN quantum well structures. *Journal of Applied Physics* 92(8):4441-4448, 2002.

[57] T. Yamamoto, M. Kasu, S. Noda, A. Sasaki. Photoluminescent properties and optical absorption al AlAs/GaAs disordered superlattices. *Journal of Applied Physics* 68(10):5318-5323, 1990.

[58] T.Y. Lin, J.C. Fan, Y.F. Chen. Effects of alloy fluctuations in InGaN epitaxial film. *Semiconductor Science and Technology* 14:406-411, 1999.

[59] L.E. Shilkrot, D.J. Srolovitz, J. Tersoff. Morphology evolution during the growth of strained-layer superlattices. *Physical Review B* 62(12):8397-8409, 2000.

BIOGRAPHICAL SKETCH

Matthias Karow was born in Gotha, Germany, where he completed his secondary education in 2007 at Gymnasium Ernestinum with a major in Mathematics and Physics. He continued his education in Physics, earning a Bachelors degree from Göttingen University in 2011 and beginning the pursuit of a Masters at the same institution with a focus on solid-state and material physics. Upon receiving a Fulbright Scholarship, Matthias joined the QESST ERC and the Electrical Engineering department at Arizona State University in 2012, from which he earns a Masters degree in Summer 2014. He is a member of the HKN Engineering Honor Society, IEEE, and the German Physical Society.